Search for Periodicity in Emission of Very High Energy Gamma-Rays from the Supernova Remnant MSH 15-52

Isak Delberth Davids

B. Sc (Honours)

Thesis submitted in the Unit for Space Physics of the North-West University in partial fulfillment of the requirements for the degree Magister Scientiae

Supervisor: Prof B. C Raubenheimer

Potchefstroom, South Africa
April 2007

Search for Periodicity in Emission of Very High Energy Gamma-Rays from the Supernova Remnant MSH 15-52

Isak Delberth Davids

B. Sc (Hons)

Thesis submitted in the Unit for Space Physics of the North-West University in partial fulfilment of the requirements for the degree Magister Scientiae

Supervisor: Prof. B. C Raubenheimer

Potchefstroom, South Africa
April 2007

Abstract

For the first time in the history of very high energy γ-ray astronomy, diffuse emission of γ-rays from a pulsar wind nebula, was observed from the supernova remnant, MSH 15-52, by the H.E.S.S., in 2004. Along with MSH 15-52, H.E.S.S. discovered very high energy (VHE) γ-ray emission from 14 extended pulsar wind nebulae (PWNe) in a Galactic plane survey. Furthermore, H.E.S.S. (High Energy Stereoscopic System) found no pulsed VHE γ-ray emission from 13 young pulsars *at their radio periods.*

The supernova remnant (SNR), MSH 15-52, consisting of a PWN which is powered by a $\sim$ 150 millisecond relatively young and energetic pulsar, B1509-58, was observed with H.E.S.S. during 23 nights. The likelihood of the pulsar periodicity being propagated into the PWN emission was investigated, by searching for periodicity of VHE γ-ray emission *at and near the radio period* from the entire composite supernova remnant. An exhaustive approach, using Fourier analysis techniques were employed for searching for a pulsed signal. This was done via the well-known universally most powerful (UMP) test, the Rayleigh test, and the H-test.

No coherent sinusoidal pulsed emission, with $> 1\%$ signal strength, could be seen using the Rayleigh test, between 151.282 and 151.301 ms, in observations with a 120 minute average duration. The Eadie combination method of Rayleigh test results, also showed no evidence of strong flares or non-coherent pulsed emission between 151.277 and 151.301 ms, during a night observation. No coherent pulsed signal with signal strength of $> 0.3\%$, between 151.288661 and 151.288675 ms, was detected with the application of the Rayleigh test on the 3.9 month bulk data. Moreover, the H-test proved that there was no presence of any non-sinusoidal pulsed emission, again between 151.282 and 151.301 ms, during a night observation. Therefore, no pulsed VHE γ-ray emission was detected from the supernova remnant MSH 15-52 *at and near the pulsar radio period.*

NORTH-WEST UNIVERSITY
YUNIBESITI YA BOKONE-BOPHIRIMA
NOORDWES-UNIVERSITEIT

Opsomming

Vir die eerste keer in die geskiedenis van baie hoë energie γ-straal astronomie, is diffuse hoë energie γ-straling van 'n pulsaar newel wind, in 2004 waargeneem met H.E.S.S, vanaf die supernova res, MSH 15-52. Nog 14 ander uitgebreide newels, saam met MSH 15-52, is in 'n Galaktiese soektog van baie hoë energie (BHE) γ-straal bronne ontdek deur H.E.S.S (Hoë Energy Stereoskopiese Siesteem). Verder het H.E.S.S. 13 jong pulsare waargeneem, en geen periodiese BHE sein *by hul radio periodes* gekry nie.

Die supernova res (SNR), MSH 15-52, bestaande uit 'n pulsaar newel wind (PNW) wat bekragtig word deur 'n jong energieke $\sim$ 150 millisekonde pulsaar, B1509-58, was waargeneem deur H.E.S.S. (Hoë Energie Stereoskopiese Siesteem) gedurende 23 nagte. Die waarskynlikheid dat die pulsaar se periodisiteit voortgeplant word na die PNW, is ondersoek *op en rondom die radio periode*, deur die hele saamgestelde supernova res te bestudeer. 'n Breedvoerige benadering wat van Fourier analise gebruik maak, was toegepas om na 'n gepulseerde sein te soek. Dit is met die bekende uniform mees kragtige toets, die Rayleigh toets, en die H-toets gedoen.

Geen koherende sinusvormige gepulseerde straling, met $> 1\%$ sein sterkte, is tussen 151.282 en 151.301 ms, in 'n tipiese 120 minute waarneming met behulp van die Rayleigh toets gesien nie. Die Eadie kombinering van die Rayleigh toets se resultate het geen getuienis van 'n sterk opflikker of nie-koherente gepulseerde sein, tussen 151.277 en 151.301 ms, gedurende 'n nag se waarneming gelewer nie. Geen nie-koherende gepulseerde straling met $> 0.3\%$ sein sterkte, tussen 151.288661 en 151.288675 ms, is gekry deur die Rayleigh toets op die hele 3.9 maande se data toe te pas. Verder het die H-toets bewys dat daar geen teenwoordigheid van enige nie-sinusvormige gepulseerde straling, weereens tussen 151.282 en 151.301 ms, gedurende 'n nag waarneming was nie. Dus is daar geen gepulseerde BHE γ-straling *op en rondom die radio pulsaar periode*, vanaf die supernova res MSH 15-52 waargeneem nie.

Contents

List of Figures

Acronyms used

Each of the following listed abbreviations will be written out in full the first time it appears within the main text.

Those abbreviations that appear only once are not listed.

ACT	Atmospheric Cherenkov Technique
ATNF	Australia Telescope National Facility
CMBR	Cosmic Microwave Background Radiation
CR(s)	Cosmic Ray(s)
CT	Cherenkov Telescope
EAS	Extensive Air Shower
IC	Inverse Compton
IACT	Imaging Atmospheric Cherenkov Technique
IFS	Independent Fourier Spacing
ISM	Insterstellar Medium
LGM	Little Green Men
MJD	Modified Julian Day
PSR	Pulsator Radio Source (Pulsar)
PWN(e)	Pulsar Wind Nebula(e)
SNR(s)	Supernova Remnant(s)
SSB	Solar System Barycentre
ToA(s)	Time(s)-of-Arrivals(s)
VHE	Very High Energy

Chapter 1

Introduction

> "Admittedly, we play a considerable role in what happens in the near vicinity of Earth — by our technical achievements and mental insights — but we do not really play a role that would upset the Universe. We are rare, but not central, and not forbidden" — Kundt (2004)

1.1 Men's Curiosity

THE Universe that we reside in, offers fascinating yet unprecedented features. The planet Earth that we live on, may *not* take a crucially outstanding part in the entire Universe, but we are continuously affected by the activities that takes place elsewhere in the Universe. Astronomy and astrophysics are such studies driven by the motive to gain better insight into the functioning of the Universe. In experimental physics, one can manipulate the conditions of the objects that is being studied, order to test the formulated laws of nature. This however, is not possible in astronomy and astrophysics, bodies that are studied are beyond reach and beyond control of the researcher — the laws of nature can only be induced from observing energy transfers in the Universe. The fact that astronomers and astrophysicists cannot conduct controlled laboratories for stellar objects, makes this field highly dynamic and very exciting, as well.

Energy is a very essential quantity that is ever in transit in the Universe. The amount of electromagnetic energy involved in an activity is descriptive of the plausible physical processes involved therein. Hence it is worthwhile to subdivide electromagnetic energy in some sensible energy ranges — the electromagnetic spectrum. The major electromagnetic energy divisions, in an increasing order of frequency, go from radio, microwave, optical, to gamma-rays. Gamma-ray astronomy is thus a division of astrophysics that concerns itself primarily with the relatively high energy types in the Universe.

Gamma-ray astronomy deals with astrophysical energies between just less than 30 MeV to about 30 PeV. This field is subdivided into branches again according to energy intervals as shown below (Aharonian, 2004) in Table 1.1.

Branch of Gamma-Ray Astronomy	**Energy range**
Low Energy (LE)	< 30 MeV
High Energy (HE)	$\sim$30 MeV to $\sim$30 GeV
Very High Energy (VHE)	**$\sim$30 GeV to $\sim$30 TeV**
Ultra High Energy (UHE)	$\sim$30 TeV to $\sim$30 PeV
Extremely High Energy (EHE)	> 30 PeV

Table 1.1: *The different branches of γ-ray astronomy as defined by Aharonian (2004)*

The last energy domain, the EHE, has not yet seen significant investigated sources. This is partly attributed to the very small *mean free paths* (only 8.5 kpc for a 1 PeV photon) that γ-rays of those energies have compared to huge mean free paths (longer than the Hubble size of the Universe) for typical GeV γ-rays (Aharonian, 2004). These short mean free paths of EHE γ-rays mean that the frequent collisions it encounters does not allow free propagation when entering our Galaxy.

The Galactic center is roughly 8 kpc from us, while the Galactic diameter is about 30 kpc. With that it looks fairly difficult to see a PeV γ-ray from a extragalactic source, hence the Universe has been relatively 'dark' through UHE and EHE eyes. However, TeV γ-rays can be seen as far as 10^5 kpc, while the visibility range for EeV γ-rays is 10^4 kpc (Aharonian, 2004). We can see that VHE γ-ray emission form part of the highest energy forms that can be observed from Earth. Our work falls under this category and is an attempt to contribute, even at the smallest degree, to the insight into the VHE γ-ray phenomena in some astronomical objects.

Supernovae are very dramatic and highly energetic explosions that marks the end of the life-time of a star. Extra-ordinarily huge amounts of energy is released in such an explosion, hence these events may be responsible for the acceleration and perhaps the origin of the now close to 100 year old mystery of the origin of Cosmic Rays (CRs), since their discovery by Victor Hess in 1912. Hess received the Nobel Prize in Physics in 1936 for his discovery of CRs.

Perhaps the most important agent in astrophysical studies is electromagnetic radiation. Astrophysical bodies emit electromagnetic radiation in various forms. Scientists have to capture and analyze these signals in order to understand the very object that the radiation comes from. Extra-terrestrial high-energy radiation from outer space enters the Earth's atmosphere, and as such, humans and earthly material are exposed to these

radiation on a continual basis. Even though it may not seem to be immediately detrimental, long term exposures have the ability to affect living organisms. The effects can be negative — like when cancer is induced by cell mutation. The effects become more pronounced when we consider astronauts that leave the Earth's atmosphere and magnetosphere with spacecraft and other space missions. In other earthly industries, engineers and scientists artificially propel atomic particles to high speeds in order to create high various energies that the industry requires. The resulting high-energy radiation is useful, yet it can be hazardous to human life. Whether natural or man-made, it is inevitable to understand the creation mechanism, properties and behaviour of radiation in order to satisfactorily deal with the risks that it may pose to life.

1.2 The "Little Green Men"

In the late 1960s, at the Cambridge University in Britain, a student, Jocelyn Bell, and her academic mentor, Antony Hewish, built a 3.7 m wavelength radio telescope array for the purpose of investigating astronomical scintillation. Their studies were concerned with rapid variations in apparent brightness in the planetary system. The experiment was also used to study high-frequency fluctuations of radio sources (Wikipedia, 2006c). Surprisingly enough, they picked up radio signals that were so extra-ordinarily periodic that they reckoned that some extra-terrestrial life is in communication with them. The first suspicion was that the radiation must be from some *Little Green Men* (LGM) — from somewhere outside our terrestrial vicinity.

But the idea of the LGM did not survive for long, and the idea that these are natural phenomena advanced. Astronomical bodies from which these radio pulses were observed were called *pulsating radio sources* — or a PULSARs for short. Pulsars were a serendipitous discovery. Hewish, Bell and colleagues announced early in 1968, the discovery of the first pulsar PSR 1919+21 (Manchester & Taylor, 1977). The prefix PSR represents the term pulsar. The Nobel Prize for Physics for 1974 was awarded to Hewish and a fellow radio astronomer Martin Ryle for the discovery of pulsars[1] and the associated technical work (Wikipedia, 2006a).

1.3 Cherenkov Effect

The Earth's atmosphere serves as an excellent 'messenger' of the arrival of VHE γ-rays at Earth. When an incident TeV γ-ray enters the Earth's atmosphere it interacts with atoms and molecules in the air resulting into a cascade of secondary charge particles continuing the journey down to the surface of the Earth. These

[1] Reports are that the prize awarded to Hewish was regarded by some as controversial, as Bell was the first to notice the pulsating stellar radio object

extensive air shower (EAS) of charged particles may travel at relativistic speeds in air — displacing and polarizing the ambient air molecules along their way. In the process of restoring their equilibria the air molecules emit photons. The photon emission travels in the form of faint blue light down to the Earth's surface. This $\sim$ 10 ns duration light pulses, not visible to the naked eye, is called *Cherenkov radiation.* The light arrives on the Earth's surface in a conic structure — a pool of about 200 m diameter. Cherenkov light was named in honour of the Russian physicist Pavel Cherenkov, who received the Nobel Prize for Physics for 1958 for his discovery, way back, in 1934 of this effect in water when it is exposed to radioactive bombardment (Wikipedia, 2006f).

Since the incident direction of the initial VHE γ-ray is maintained by the symmetry of the EAS and the Cherenkov light cone, it is possible to reconstruct the line pointing to the source of the VHE γ-ray if sufficient light is detected. The tracing of the origin of a γ-ray is so convenient because γ-rays travel undeflected by magnetic fields — their trajectories are straight. The process of reconstructing the incident direction of a γ-ray using the Cherenkov light, of which details are given by e.g. Jelley & Porter (1963), is called the *atmospheric Cherenkov technique* (ACT). A telescope system that is utilized for the ACT is called a Cherenkov telescope (CT). The detection procedure is based on the use of a photomultiplier to create a pulse from a photon arrival. By using multiple photomultiplier tubes one can create an image of the shower — a technique known as the *imaging atmospheric Cherenkov technique* (IACT). The determination of the arrival direction can be largely enhanced by positioning several CTs at optimum separation distances, of between 70 and 140 m (Hofmann et al., 2000), and performing the reconstruction of the γ-ray incident direction with all concurrently triggered CTs. This technique which requires triggering of at least two CTs is known as *stereoscopic imaging*, and is discussed in detail by e.g. Aharonian & Konopelko (1997). Due to the large collection area required, considering the $\sim$100 m Cherenkov light pool, these telescopes are basically ground-based.

1.4 The H.E.S.S. Experiment

Recently, in 2004, a high technology third-generation Cherenkov detector array has been commissioned in Namibia (Hinton, 2004). Pictured in Figure1.1, the system has a name almost in resemblance to the man who discovered CRs, Victor Hess — it is called the *High Energy Stereoscopic System* (H.E.S.S).

Presently H.E.S.S., consists of four 13 m diameter CTs each with a mirror area of about 107 m^2 and a 5° field of view. The camera host 960 photomultipliers, where each serve as a 0.16° pixel (Hinton, 2004). These attributes gives the system a greatly enhanced detection sensitivity (in comparison to previous telescopes) and lowers the energy threshold for it to observe γ-rays in the energy domain to just above 100 GeV. The

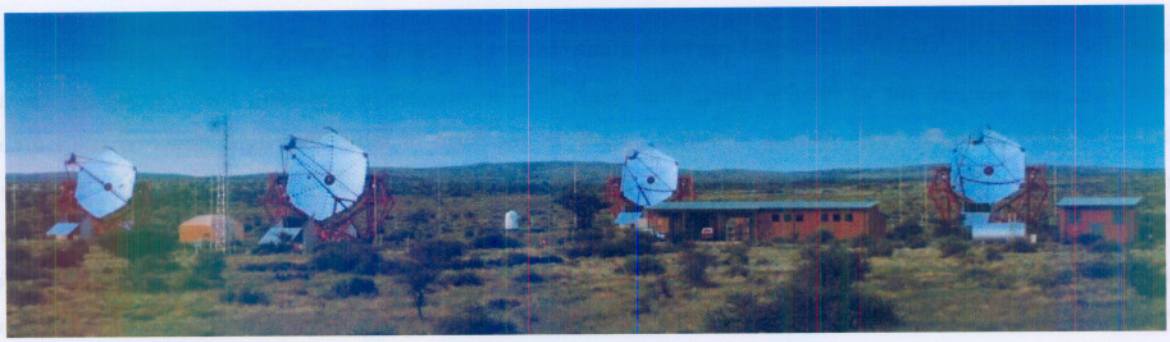

Figure 1.1: *A picture of the H.E.S.S. telescopes (see H.E.S.S. website). The four telescopes seen here, are arranged in a square array.*

system has overwhelmingly contributed in cosmic γ-ray astronomy since its commissioning a mere three years ago. Recently, Weekes (2005) noted that:

> The catalog of current sources listed in ...is dominated by HESS results; it is a measure of their success that they have been able to announce a new discovery every month and no end appears to be in sight.

For example, H.E.S.S. is the first experiment that resolved the morphology of the supernova remnant MSH 15-52 in γ-rays (Aharonian et al., 2005a) — the very source that we are interested in.

Plans are currently underway to introduce an additional spherical mirror with a diameter of about 30 m. This fifth CT will be located on the center of the 120 m square, with the existing four CTs positioned on the vertices. This large light collector is planned to have a mirror area of 596 m^2 with a 3.5° field of view (Vincent, 2005). For those directly involved this envisaged phase will mean intense activity in γ-ray data analyses, while for the public hopefully it will mean broadening of our understanding of the Universe.

1.5 Mission of the Project

The rotational energy of a pulsar is dissipated into a magnetized relativistic wind consisting of electrons and positrons. (Reynoso et al., 2004). When the pressure from the ambient interstellar medium (ISM) causes a termination of this relativistic wind, a luminous pulsar wind nebula (PWN) is produced. The pulsar is then said to be associated with the PWN.

A typical well-known example of such an association is the supernova remnant MSH 15-52, in which the young (about 1700 year old) energetic pulsar B1509-58 powers an elongated pulsar wind nebula around it. This project is based on studies carried out on VHE γ-ray emission from this association.

The morphology and behaviour of a pulsar wind nebula is strongly dependent on the enclosed pulsar. It is therefore likely that the attributes of each PWN can be traced back to the behaviour of the associated pulsar. In fact, the number of PSR-PWN associations has recently increased by virtue of the H.E.S.S. survey of the Galactic plane. This survey that began in 2005, reveals VHE γ-ray emission from a total of 14 extended nebulae (Gallant, 2006) — 10 of these sources are new discoveries. The other four sources that were detected in VHE energies are the Crab, Vela, MSH 15-52, and G0.9+0.1 supernova remnants.

Of the 10 newly discovered VHE γ-ray sources, 6 appear to be associated with pulsars (Gallant, 2006). Four of the newly discovered VHE emitters, and the already known SNR G0.9+0.1, are not yet associated with pulsars.

Central to an articulate understanding of the origin, evolution and dynamics of supernova remnants, is the question — do pulsars induce their periodic nature in the winds that they produce? Of the 14 VHE γ-ray detections of H.E.S.S. mentioned above, more than 60% are believed to be driven by pulsars — so it is plausible to argue that pulsar emission is closely related to the emission by the associated PWN. The driving force behind this project is to explore the mutual relationship in a pulsar-PWN association, through the analysis of their emission frequency.

We investigated the presence of any periodic VHE γ-ray emission from MSH 15-52, close to the known radio period of PSR B1509-58. The data analyzed were acquired in the year 2004 by the H.E.S.S. experiment.

In Chapter 2, we give the reader some theoretical background on supernova remnants and pulsars. We also introduce the supernova remnant MSH 15-52, and the pulsar B1509-58. Chapter 3 outlines statistical inference methods as applied in γ-ray astronomy. The structure of the acquired data as well as the standard data reduction and preparation techniques are discussed in Chapter 4. The results from the statistical analyzes are given in Chapter 5. In the last chapter we summarize the results and draw conclusions.

Chapter 2

Pulsar Physics

> "Clearly distinguishable pulses showing periodicity were recorded on November 28, 1967. During the next eight weeks Hewish and his colleagues systematically eliminated all of the more plausible explanations for the strange signals." — Manchester & Taylor (1977)

2.1 The Birth of a Neutron Star

2.1.1 Hydrostatic Equilibrium

THE life-cycle of a star can enter a stage at which it suffers a violent explosion, initiating thereafter other spectacular astrophysical phenomena. During the greater part of its life time a typical star keeps itself in equilibrium, avoiding an explosion by burning its fuel from within. These fueling processes constitute the fusion reactions that convert the initially abundant hydrogen into helium, helium into carbon, and so on, up to the formation of iron nuclei. The reactions releases energy that heats up the gas, which responds by expanding, thus generating internal gas pressure. The pressure from these nuclear processes counteracts the ever-existing tendency of a gravitational collapse onto itself. Therefore the process maintains the *hydrostatic equilibrium* of the star, see e.g. Shklovskii (1978), such that the star remains for millions of years as a ball of gas with no net significant contraction or expansion.

However, the nuclear fuel can be exhausted at some stage, thus extinguishing the nuclear furnace, which implies that the internal pressure fades away. With this imbalance the star will collapse under influence of gravity onto itself. This happens as the outer layers of the star can no longer resist the gravitational force,

which pulls the outer matter inwards. Depending on the massiveness of the infalling matter, the collapse can be followed by a enormous rebound action that violently ejects much of the stellar material into the *interstellar medium.* This process constitutes a *supernova* (SN) explosion.

The term supernova is in fact a misnomer as it was originally meant to refer to a 'new' stellar object, but in essence this is an existing stellar body at a dramatic stage of its life-cycle. However, the sudden increase in the light output, which fades away with time, makes it look as if a 'new' brighter star has appeared in the sky, hence the misnomer. The particular type of explosion that we just described is called the TYPE II supernova. The events that will transpire after the SN explosion over hundreds or thousands of years and the associated products are prescribed by the mass of the star.

2.1.2 Degeneracy Pressure

For those stars with mass less than 10 solar masses (10 $M_{\odot}$) the system gradually cools to eventually become a white dwarf. During its subsequent lifetime this white dwarf, if involved in a binary association, may accumulate material from a companion star through accretion. This process can result in another type of thermonuclear SN explosion, a TYPE I supernova, if the white dwarf reaches its *Chandrasekhar limit* as explained by e.g. Tayler (1994) and Wikipedia (2006g). The observational difference between the TYPE I and II supernovae is in their optical spectra. At their maximum brightness TYPE I supernovae do not show hydrogen Balmer lines, whereas a TYPE II supernova generally does (NASA, 2006).

For even more massive stars the fusion reactions of heavier nuclei can be ignited, by even more increase in the internal temperature due to the greater gravitational collapse. Depletion of the fuel supply in the star causes contraction of these regions, which in turn increases the temperature until the next series of nuclear burning gets ignited (Tayler, 1994). These develops the star's interior into concentric layers of progressively heavier atomic nuclei build out from the center. Iron is the heaviest atomic nucleus that can be achieved, and thus an iron core is formed.

Any furher collapses will increase the density of the star. However, electrons cannot occupy identical quantum states, thus the matter becomes *degenerate.* The latter being the consequence of the *Pauli exclusion principle* — free electrons cannot be packed closely together anymore. If this situation is kept then we have a white dwarf which is being prevented from further shrinking by the so-called *degenerate electron pressure* in the stellar interior (e.g. Kawaler et al., 1997). However in other cases, with greater masses, this constraint can be lifted by combining an electron with a proton to form a neutron. This may happen until the star to predominantly comprise of neutrons — the birth of the neutron star.

2.1.3 The Pulsar

A neutron star is one out of the several known endpoints of stellar evolution, and is maintained by the *degenerate neutron pressure*. They are relatively small objects with radii between 10 and 20 km. However a neutron star can have a mass anywhere between 1 to about 2 solar masses. Thus these are extremely dense astronomical bodies with typical densities in the range 10^{10} to 10^{12} kg/cm^3 (Wikipedia, 2006e). A neutron star will rotate around an axis with very fast rotation speed — the rotation that is a direct result of angular momentum conserved after the explosion. We say 'fast' rotations, because in some cases a neutron star can make a revolution in a fraction of a millisecond.

A pulsar is a magnetized fast-rotating neutron star, which is in essence a collapsed core of a massive star. We assume a dipolar magnetic field model, around a spherical body. Their crust consist mainly of heavy metals like iron, which encompasses an incredibly dense neutron matter. Pulsars initially resides in an associated SNR.

Types of Pulsars

Pulsars can be subdivided into at least three groups depending on the source of the energy that powers the observed radiation.

↪ ROTATION-POWERED PULSARS

For these pulsars the energy lost through rotational motion is emitted as radiation. Therefore this class of pulsars spin speed is gradually decreases over time. Millisecond pulsars are typical members of this class. These objects are commonly simply referred to as pulsars, and can be so periodic that they are also regarded as *astronomical clocks*.

↪ ACCRETION-POWERED PULSARS

Neutron stars of this class accrete matter from companion stellar objects via strong gravitational pull. Hence, they exist in binary systems. The gravitational potential energy of the accreted matter is the source of the radiation. Most X-ray pulsars belong to this group — also called X-ray bursters.

↪ MAGNETARS

Magnetars have extremely strong magnetic fields — of up to $\sim 10^{11}$ T (Wikipedia, 2006d). The decay of this field powers the radiation. The magnetic field is about 10^{15} times greater than the Earth's magnetic field, assuming $\sim 10^{-4}$ T for the latter.

A pulsar is an interesting object of which emission from it were initially mistaken for communication signals coming some extra-terrestrial fellows — the LGM. When a fast spinning neutron star emits radiation in a beam, a distant observer can only see the radiation at times when the beam passes the line of sight to the neutron star. Such pulsating emission or pulses are periodic, can be spaced with excellent precision at periods between a few milliseconds and several seconds. Pulsars are believed to be primarily powered by their rotation. The radiation emitted along its magnetic axis sweeps out a beam of radiation, like a lighthouse, as it rotates. We observe a pulse each time the beam passes our line of sight to the pulsar. Thus we observe emission of electromagnetic radiation at the pulsar rotation period. The pulsar emits the lost rotational kinetic energy through radiation, the process better known as the pulsar *spin-down*. Tiplady & Frescura (2002) discuss the time-dependent evolution of the spin-down in detail. These very accurate astronomical clocks are objects of considerable interest to this project.

If the degenerate neutron pressure is not sufficient to sustain the hydrostatic equilibrium, further gravitational collapse can take place producing a *black hole* — a concept not of concern to this project.

2.2 Post-Explosion Radiators

2.2.1 The Remnant & the Wind

A supernova remnant (SNR) is the entire structure resulting from a violent stellar explosion, including the pulsar. The structure continually expands into the ambient environment, causing an evolution of series of astronomical activities. It is bounded by a shockwave that is expanding into the ISM as it evolves. The shockwave is a result of stellar material accelerated to speeds greater than the speed of sound in that medium, causing a shockwave that propagates radially outwards from the central pulsar.

A typical SNR comprises of the supernova ejecta (the stellar material expelled during explosion) and the interstellar material that it shocks along its expansion. Due to the enormous energies involved in the explosion, the ejecta gets huge initial spatial velocities that can reach $\sim 10^3$ km/s. It is this high energy thrusting through the ISM, that forms a shock wave that heat up the ambient gas material to $\gtrsim 10^6$ K. The result is an accelerated relativistic plasma wind in the ISM. We will here deal with the case where the central stellar powering object is a pulsar produced by the processes as described in the previous section. As outlined by Amato (2003), if the surrounding SNR confines this magnetized wind, then the energy loss from the central pulsar can be observed as non-thermal radiation which forms a 'cloud' around the pulsar — the so-called *pulsar wind nebula* (PWN).

Due to the spherically symmetric geometry of a SN, the pulsar is initially located at the center of the supernova shell. In case of any asymmetry in the SN explosion, the pulsar will have some spatial velocity up to $\sim 10^3$ km/s into some preferred direction. This speed is greater than the spatial speed of the progenitor star — implying a 'kick' given to the pulsar at the time of the explosion.

SNRs can have different morphologies. Some show a shell type of morphology, like Tycho's and Kepler's SNRs (Gaensler & Slane, 2006). A *shell-type* SNR depicts a centrally empty ring like shell. Others have central regions that radiate light at various wavelengths, like the Crab Nebula. The latter type of SNRs have pulsars at their centers and are also called *Crab-like*. In the case of a combination of the two types, where a shell-like SNR is surrounded by a PWN the system is referred to as a *composite system*. A good example of a composite system is the supernova remnant MSH 15-52 (Khélifi et al., 2005), which host a relatively young and fast spinning pulsar B1509-58 — an interesting system that will be further dealt with in this project.

2.2.2 Emission Regions

Since a pulsar and its nebula can both be observed in either radio, X-rays and or γ-rays, we can argue that the pulsar and its PWN are both emitters of electromagnetic radiation. A perfect example of such an association is the pulsar B1509-58 which resides in the supernova remnant G320.4-1.2. This association is the third such case identified after the Crab and Vela Nebulae cases (see e.g. Gaensler et al., 2002). However, at present H.E.S.S. has brought the total number of such associations to around ten.

For pulsars, there are currently two major scenarios explaining where emission regions are located. The two models that customarily describe these regions are, the *polar cap* and the *outer gap* models.

↪ The Polar Cap Model

The polar cap is the region near the surface of a neutron stars magnetic pole (see Figure 2.1). This approach considers electric fields (above the polar cap) induced by rotation, as being responsible for particle acceleration (see e.g. Daugherty & Harding, 1982). The accelerated particles then make their way out along the curved open magnetic field lines.

↪ The Outer Gap Model

The outer gap refers to the region bounded between the most outer closed field line and the polar cap (see Figure 2.1). This is the region near the so-called 'null' surface. The null surface is defined by the region in which $\mathbf{\Omega} \cdot \mathbf{B} = 0$, where the magnetic field is represented by $\mathbf{B}$ and the rotation vector by Ω. As described by e.g. Cheng et al. (1986), this model regards electrodynamical measures as responsible for particle acceleration from the outer magnetospheric regions of the pulsar.

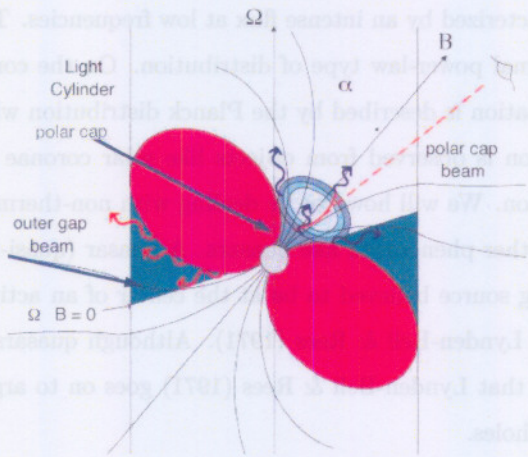

Figure 2.1: *A schematic view of the polar cap and outer gap emission regions of a pulsar (image taken from Schmidt, 2005). The outer gap region is located outside the last closed field line, while the polar cap region is at the magnetic pole of the pulsar. The vertical lines defines the light cylinder.*

Radio emission have been and is the dominant energy band radiated by pulsars and nebulae. Thus radio astronomical knowledge is the cornerstone in many regards when examining these sources. Much of the information that is and will be presented in this work, establish itself from radio emission measurements.

The emission from a astrophysical body can be described by its spectrum, i.e. the variation of radiation intensity over a range of observed frequencies. In radio astronomy, if we define the flux density as the power received from the source per unit frequency per unit area, then it is commonly accepted that, see for instance Pratap & McIntosh (2005), given the flux density S_ν for a particular frequency ν, the two are related by

$$S_\nu \propto \nu^s \tag{2.1}$$

where s is the *spectral index*. For higher energy astronomy studies (say X-ray and γ-ray studies) the concept of the *photon index* is used (Gaensler & Slane, 2006). In the latter case, given the number of emitted photons with energy E as N_E, the photon index Γ describes an analogy to Equation 2.1 as

$$N_E \propto E^{-\Gamma} \tag{2.2}$$

These relationships, Equations 2.1 and 2.2, basically describes the power distribution in the emitted frequencies. The spectral index is an important variable as it can give an indication of the type of dominant radiation present in terms of it being being *thermal* or *non-thermal*. The flux density of thermal radiation

tends to either increase with or remain constant with increasing frequency (Pratap & McIntosh, 2005), while non-thermal radiation is characterized by an intense flux at low frequencies. The radiation energy spectrum of a SNR assumes a non-thermal power-law type of distribution. On the contrary, as stated by Pratap & McIntosh (2005), thermal radiation is described by the Planck distribution which has a strong temperature dependence. Thermal radiation is observed from objects like solar coronae and accretion disks — corresponding to blackbody radiation. We will however be dealing with non-thermal radiation which apart from SNRs, is also observed from other phenomena like quasars. A quasar (quasi-stellar object) is a massive, of the order of 10^8 $M_\odot$, powering source believed to be at the center of an active galactic nucleus (AGN), as can be seen from the work of Lynden-Bell & Rees (1971). Although quasars are outside the scope of this work, it is interesting to note that Lynden-Bell & Rees (1971) goes on to argue that 'dead' quasars at the nuclei of galaxies forms black holes.

2.2.3 Emission Mechanisms in SNRs

Energetic radiation from stellar objects can be attributed to various physical processes that takes place in, on and around such an object. The following are the currently known processes that are held accountable for production and acceleration of high-energy radiation in astrophysical bodies.

↪ SYNCHROTRON RADIATION

Fundamental physics requires that accelerating charges must radiate. Charged particles are also required to spiral around magnetic field lines, hence they accelerate. Synchrotron radiation refers to the radiation emitted by extreme relativistic charged particles that gyrate around magnetic field lines. The radiation can typically be radio, optical, X-rays or γ-rays. For example the Crab nebula has a continuum synchrotron radiation spectrum, where its relativistic electrons loose energy by radiation, but gets re-powered by the central Crab pulsar. The term *curvature radiation* is also used referring to the radiation from charge particles that exhibit curve-like motion around field lines. The perception that pulsars are highly magnetized neutron stars, supports the notion that synchrotron radiation be a plausible radiation mechanism in pulsar magnetospheres. The spectrum that result from synchrotron emission has a power-law distribution, with a more pronounced flux density for low frequencies (Pratap & McIntosh, 2005).

↪ INVERSE COMPTON RADIATION

When highly relativistic electrons collide with low energy photons, the energy transfer converts the latter into high-energy photons. This process that can easily turn a soft photon into a γ-ray, is called inverse Compton (IC) scattering. IC scattering is as such associated with high-energy γ-ray production within pulsar regions. The relativistic electron in this case could be from the pulsar or SN ejecta, whereas the target low-energy photon can come from the ambient *cosmic microwave background radiation* (CMBR).

The CMBR, which is believed to be a 2.7 K isotropically distributed evidence of the *big bang*, fills the Universe uniformly such that the availability of low-energy photons is not a great concern. This creation of a high-energy photon is called 'inverse' Compton scattering, to distinguish it from Compton scattering where an incident high-energy photon transfers its energy to a low-energy electron. If the low-energy target photon is a product of a synchrotron radiation (emitted as explained above by gyrating energetic electrons) then the process gets renamed to the *synchrotron self-Compton radiation.*

↪ BREMSSTRAHLUNG

An energetic, light, charged particle — like an electron — can interact with a heavier particle when the two come close to each other. The electric field of the heavier particle can accelerate (or decelerate) the electron. But from fundamental physics it is known that accelerating particles are bound to radiate. Such radiation due to the acceleration of a charged particle in the Coulomb field of another charged particle bears the name Bremsstrahlung meaning 'braking radiation'. It is alternatively also known as the *free-free* emission. In the astrophysical sense, the electrons in the ionized plasma encounters the nuclei of the medium they propagate through.

↪ ANNIHILATION

An anti-particle is defined by the opposite quantum number (e.g. the charge) that it has in relation to some particle. However, a particle and its anti-particle can undergo a collision where the total momentum, energy, and quantum numbers are conserved. If the initial quantum numbers are opposite the product can be a particle with a zero quantum number — like a photon. When an electron and an anti-electron annihilates, the product is a γ-ray photon. In this case the quantum number of a particle is represented by the respective charge. Therefore the charge conservation ensures that the two equal and opposite charges in an electron-positron annihilation produces a neutral γ-ray. The reverse reaction, in which a γ-ray creates an elementary particle and the corresponding anti-particle, is called *pair production.*

↪ LINE EMISSION

When an electron undergoes a transition between two quantum levels in an atom, the energy difference is emitted in the form of photons (Ueno, 2005). This emission is known as *line emission* or alternatively as *bound-bound* emission. In the astrophysical sense, this phenomenon takes place during occasional collisions of ionized plasma with electrons. The excitation of the ionized plasma triggers energy level transitions.

These emission mechanisms can be present in astrophysical bodies in various proportions. Some mechanisms are more dominant in certain scenarios. For example the inverse Compton-scattering and synchrotron radiation are believed to be largely responsible for γ-ray emission from SNRs.

Using the "standard candle" of VHE γ-ray astronomy (the Crab Nebula), it is observed that SNR emission between radio and about 1 GeV energy γ-rays generally originate from synchrotron radiation from relativistic

electrons and positrons accelerated by pulsars — while the VHE γ-ray emission above 1 GeV is interpreted as resulting from inverse Compton scattering by the same accelerated electrons and positrons (Gallant, 2006).

2.3 Basic Pulsar Physics

2.3.1 The Pulsar's Spin-down & and the Pulsar Age

The laws of physics have been fairly well tested in the studies of pulsars[1]. Let us consider an *isolated* pulsar which has a spin period P with a frequency ν (where $P = \nu^{-1}$). The angular frequency is then defined by $\omega = 2\pi\nu$. The measure of a pulsar's age since the explosion is given by the parameter called the *characteristic age*, denoted by τ_c. Pulsars convert rotational kinetic energy E_{rot} into luminosity. This power radiated, $\dot{E}$, is better known as the spin-down luminosity, the terminology inspired by the fact that the radiation continuously reduces the spin speed of the star. The relation between the spin-down luminosity and rotational kinetic energy is (Gaensler & Slane, 2006)

$$\frac{d}{dt}E_{rot} = -\dot{E} \tag{2.3}$$

The loss of energy over time means that the pulsar must have a non-zero period derivative with respect to time, $\dot{P} = \frac{dP}{dt}$. In fact the spin-down increases the pulsar period so that we have $\dot{P} > 0$ or alternatively $\dot{\nu} < 0$ at all times, except at some not so often peculiar instances called *glitches* where the opposite happens. Glitches are highly fascinating pulsar events, however we defer its discussion to a later stage.

Denoting the pulsar's moment of inertia by I which is $\sim 10^{38}$ kg m^2 (Gaensler & Slane, 2006, note the error in the units given therein), we can write down the rotational kinetic energy as

$$E_{rot} = \frac{1}{2}I\omega^2 \tag{2.4}$$

so that the spin-down luminosity can be expressed using Equation 2.3 as

$$\begin{aligned} E_{rot} &= 4\pi^2 I\frac{\dot{P}}{P^3} \\ &= -4\pi^2 I\nu\dot{\nu} \end{aligned} \tag{2.5}$$

[1]The pulsar physics to be discussed herein, is primarily based on rotation-powered pulsars. Thus, the physics of other pulsating neutron stars, like accretion-powered pulsars, is not represented here

A part of the spin-down luminosity is converted into synchrotron emission in various energy bands, very commonly the radio band. If the observed luminosity in a particular energy band is L, then we can define the *energy conversion factor* in that energy interval as (Gaensler & Slane, 2006)

$$\eta \equiv \frac{L}{\dot{E}} \tag{2.6}$$

This conversion factor depends on the system under consideration, but it has been observed for some radio synchrotron emission cases that $\eta \simeq 10^{-4}$.

The spin-down effect also introduces a concept known as the *braking index*, which we will represent by n. The acceleration of particles observed in the form of a luminous outflow continuously reduces the pulsar's angular momentum — causing the *braking* of the rotational motion of the pulsar. The braking index determines the amount by which some initial value of the spin period P_0 increases to an arbitrary period value P. By definition this quantity relates the angular frequency with its first time derivative such that

$$\dot{\nu} = -\kappa\nu^n \tag{2.7}$$

where generally $2 \leqslant n \leqslant 3$, while κ is some constant determined by the magnetic dipole and the moment of inertia of the pulsar (Kaspi et al., 1994). Equation 2.7 is also known as the spin-down law. By taking yet another time derivative of Equation 2.7 and re-substituting for ν^n, we get

$$n = \frac{\nu\ddot{\nu}}{\dot{\nu}^2} \tag{2.8}$$

Once we have experimentally measured the rotation frequency and its time derivatives up to the second derivative, then Equation 2.8 becomes very useful as we can comfortably compute the braking index.

The characteristic age at some time t can also be expressed as a function of the initial period, its first derivative, the period at t and the braking index as (Gaensler & Slane, 2006; Kaspi et al., 1994)

$$\begin{aligned} \tau_c &= \frac{P}{(n-1)\dot{P}}\left[1-(\frac{P_0}{P})^{n-1}\right] \\ &= -\frac{\nu}{(n-1)\dot{\nu}}\left[1-(\frac{\nu}{\nu_0})^{n-1}\right] \end{aligned} \tag{2.9}$$

In order to find the pulsar characteristic age, we can firstly assume that the pulsar started off with a spin

speed much faster then what is observed currently i.e $\frac{P_0}{P} \ll 1$. Secondly, it is customary in pulsar studies to assume $n = 3$, for those pulsars for which the braking indices has not been measured. With these two assumptions Equation 2.9 reduces to

$$\begin{aligned} \tau_c &\approx \frac{P}{2\dot{P}} \\ &= -\frac{\nu}{2\dot{\nu}} \end{aligned} \tag{2.10}$$

However, Equation 2.10 should be seen only as an approximation as both assumptions applied on Equation 2.9 are not necessarily true and the former equation can in fact overestimate the pulsar age. Manchester & Taylor (1977) uses the initial high-velocity spatial motion of pulsars to explain that the true age can be less than the characteristic age by a factor of four.

For a pulsar with initial spin-down luminosity $\dot{E}_0$, the values of the quantities $\dot{E}$ and P evolves such that at a given time t we have (Gaensler & Slane, 2006)

$$P = P_0 \left[1 + \frac{(n-1)\,\dot{P}_0}{P_0} t\right]^{\frac{1}{n-1}} \tag{2.11}$$

and

$$\dot{E} = \dot{E}_0 \left[1 + \frac{(n-1)\,\dot{P}_0}{P_0} t\right]^{\frac{1-n}{n-1}} \tag{2.12}$$

2.3.2 The Braking Index

The braking index of a pulsar enters pulsar physics via the braking law as described in Equation 2.7 — the spin-down law. Equation 2.8, given earlier as

$$n = \frac{\nu\ddot{\nu}}{\dot{\nu}^2}$$

further simplifies the computation of the braking index, as you only need to experimentally determine the rotational frequency and it first two time derivatives. However, the values of $\ddot{\nu}$ are usually very small, $\sim 10^{-21}$ s^{-3} for the pulsar B1509-58, and consequently makes the value of n highly sensitive to any small fluctuations in the pulsar timing (Kaspi et al., 1994). The result is that values of n for many pulsars are not stable or consistent, except for a few pulsars including the PSR B1509-58.

A concept which Urama (2002b) refer to as 'anomalous' braking indices is believed to play some role in pulsar observations. These are explained by giving the spin-down law

$$\dot{\nu} = -\kappa\nu^n$$

given earlier as Equation 2.7, a closer look. The 'constant' κ is dependent on the moment of inertia I. However, I is itself not static — perhaps due to the structural evolution of the pulsar. The evolution in I is carried over to evolution in the values of n, hence the so-called anomalous braking indices.

In summary, pulsar braking indices seem not to be completely stable depending on the pulsar activity.

2.3.3 The Pulsar Interior

The commonly accepted model that describe the interior of a neutron star is given for example by Urama (2002b). It describes a neutron star with a radius of about 12 km, to consist of an outer crust of roughly 2 km, and a inner core of about 10 km. The outer crust is predominantly solid, while on the contrary the inner core is presumably made up of superfluid neutrons. This fluid of neutrons makes a superconducting fluid. It is not completely clear what material the actual center and its vicinity consist of.

In this model, the coupled lattice crust and the core are taken to be rotating at different rotation rates, perhaps due to their structural differences, resulting in a *differential rotation*. This motion leads to decoupling, causing the observed neutron star rotation to undergo sudden changes. The immediate consequences, known to date, of this phenomenon is described in the next section.

2.3.4 Pulsar Timing

Pulsars spin in a remarkably predictable manner. However, some young pulsars exhibit timing irregularities, while others are quiet in this regard. Understanding and appreciation of pulsar timing irregularities are essential when searching for evidence of periodic emission from these sources.

Although the pulsar that we study in this work, PSR B1509-58, may not have experienced some of this irregularities, it is still not exempted from such irregularities. The following can be considered as sources of timing irregularities in pulsar timing.

↪ Timing Noise

Random variations in pulse arrival times is regarded as timing noise. Timing noise can be a result of some rotational irregularities, although the physical processes associated are not well understood. Timing noise can be classified either as 'red' (low-frequency) or otherwise as 'white' noise. Livingstone et al. (2005) saw low frequency timing noise in the residuals (difference between expected and recorded arrival times) of PSR B1509-58.

Mathematically, timing noise Δ_s can be approximated with the use of the second time derivative of the rotation frequency $\ddot{\nu}$. It can be seen in e.g. Livingstone et al. (2005) that

$$\Delta_s \approx \log_{10}(\frac{\nu|\ddot{\nu}|t^3}{6}) \tag{2.13}$$

Cordes & Helfand (1980) points out that timing noise can be modelled as a random walk process, and that this timing activity is a related to the rotational energy loss of the system.

↪ Pulsar Glitches

The rotation velocity of a pulsar decreases very slowly but steadily. However, the are exceptions when a sudden variation in the spin speed is observed. These are mostly seen as sudden 'spin-ups' where the rotation instantly gets faster, called glitches. These are seen as discontinuities in the timing residuals, and have been observed in some pulsars. If the change in rotational frequency is represented by $\Delta\nu$, then a glitch is said to have a magnitude of

$$Glitch_{size} \equiv \frac{\Delta\nu}{\nu} \tag{2.14}$$

A pulsar glitch magnitude can be anywhere between 10^{-6} and 10^{-9} (Urama, 2002a). It is noted in Cordes & Helfand (1980), that the Vela pulsar experienced four large glitches of $Glitch_{size} \approx 2 \times 10^{-6}$, in a span of 10 years. On the contrary, pulsar B1509-58 is glitch-quiet — according to Livingstone et al. (2005) it has never glitched in about 21 years.

It has also been observed that after a glitch, pulsar rotation gradually normalizes back to the expected spin rate — the post-glitch recovery. This recovery processes can happen over periods of hours to years (Urama, 2002b).

Due to structural differences, the rotation speed of the outer crust of a pulsar is different from that of the deeper superconducting interior. Although fact-finding studies are still going on, a glitch is thought to result from this *differential rotation*, which causes decoupling of the two zones (Urama, 2002b). The resulting events causes 'starquakes' in the solid zone, which in turn instantly disturbs the rotation speed of the outer crust (see e.g. Urama, 2002a).

↪ Pulsar Precession

There is a perception in the pulsar physics realm, based on pulsar timing data, that some pulsars exhibit precession. Pulsar precession refers to slow small-amplitude motions of the rotational axis (Frescura,

2002). The effect is similar to the 'wobbling' action of a rotating body which has a bulged equatorial region — that is an oblate object. The Crab and Vela pulsars are amongst those pulsars that are reckoned to be precessing.

Kinematics of pulsar precession, suggesting a certain mathematical model, can be seen in Frescura (2002). The latter discusses the so-called 'free' precession of an isolated pulsar, referring to a motion not driven by gravity.

↪ 'ANOMALOUS' BRAKING INDICES

The pulsar braking index n, as discussed in § 2.3.2, is another candidate that can contribute to timing irregularities. The 'constant' κ in Equation 2.7, has been observed as changing over time, such that $\dot{\kappa} \neq 0$ (Urama, 2002b). The value of κ could be changing due to the changing moment of inertia I, or the magnetic dipole moment.

All in all, the implication is that the braking index n may vary — resulting in the so-called 'anomalous' braking indices.

2.3.5 Dynamics of the Pulsar Magnetosphere

The Pulsar Magnetosphere

Pulsars are highly magnetized stellar objects. For a relatively young pulsar (a few thousands of years old) the magnetic field strength can rise up to 10^8 T (Lyne & Graham-Smith, 1990). Such enormous fields are $\sim 10^{12}$ times the magnetic field strength of the Earth (Manchester & Taylor, 1977).Assuming a dipole field, Gaensler & Slane (2006) states that we can compute the equatorial magnetic field on the surface of a pulsar with the relation

$$\begin{aligned} B_{equator} &= 3.2 \times 10^{15} (P\ \dot{P})^{\frac{1}{2}} \\ &= 3.2 \times 10^{15} (-\frac{\dot{\nu}}{\nu^3})^{\frac{1}{2}} \end{aligned} \tag{2.15}$$

The fact that Equation 2.15 gives the magnitude of the magnetic field (in Tesla) as a function of the period and period derivative suggest that the field strength is to some extent time-dependent. Like many other stellar objects, pulsars and their immediate environments evolve over time. Therefore pulsar characteristics are generally dynamic. Pulsars possess large magnetic fields and fast rotational motion, which causes the magnetic field around it to change over time.

The spin-down energy of a pulsar is continuously emitted as electromagnetic energy into the surroundings.

The surrounding is *not* a vacuum as shown by e.g. Goldreich & Julian (1969), thus the ambient material will respond to the energy supplied by the pulsar. We can define the entire region of space in which charged particles are influenced in one way or the other by the pulsars magnetic field as the *pulsar magnetosphere*. The energy transfer via electromagnetic processes calls the study of *pulsar electrodynamics* to describe the dynamics of the pulsar magnetosphere. It is worthwhile to note at this point that we are considering the physics in which the gravitational effects are not comparable enough to the electromagnetic counterparts. To that effect, we will neglect gravitational contributions in the magnetosphere.

The pulsar magnetosphere exhibits some extent of co-rotation with respect to the pulsar's motion. Due to the huge magnetic fields, for example $\sim 10^8$ T for the Crab pulsar, there exist very large electric potentials between the polar and equatorial regions. For the Crab pulsar such potentials can be as large as $\sim 10^{16}$ V (Spitkovsky, 2005).

The Light Cylinder

The most simple intuition is that a magnetized neutron star has a dipolar magnetic field centered at the star. As such the field lines can be *closed* (leaving one pole and entering the opposite) or *open* (leaving a pole for escape to infinity). An imaginary cylinder with its sides defined to be the borders of the most outer closed magnetic field line is called the *light cylinder*. Such a hypothetical light cylinder with an infinite height is demonstrated in Figure 2.2.

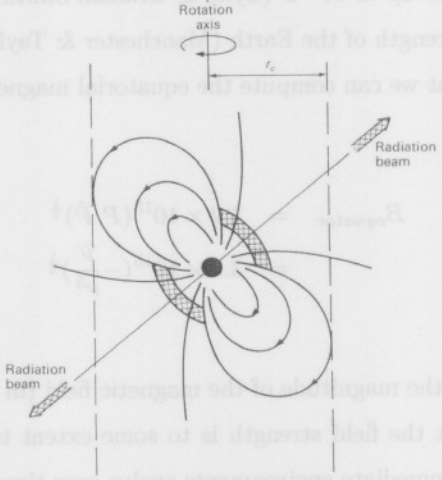

Figure 2.2: *A schematic view of the light cylinder of a pulsar (Lyne & Graham-Smith, 1990). The light cylinder is defined by the broken vertical lines, such that the radius of the light cylinder is r_c, as shown. The drawing also shows the angular off-set between the rotation axis and the magnetic axis.*

If for an arbitrary point in two dimensional spherical symmetry, r represents the radial distance from the central pulsar position and θ the polar angle measured from the rotation axis then (Goldreich & Julian, 1969)

$$\omega r sin\theta = c \tag{2.16}$$

can help us to re-define the light cylinder, where c is the speed of light. Since the part ωr represents a translational speed, we can introduce the light cylinder as the radial distance at which the rotational velocity of co-rotating particles equals the velocity of light — thus the actual name *velocity-of-light-cylinder*. We can therefore deduce that the minimum distance to the light cylinder (with $\theta = \pi/2$) goes like

$$\begin{aligned} r_c &= \frac{c}{\omega} \\ &= \frac{cP}{2\pi} \end{aligned} \tag{2.17}$$

where the second equality comes from the use of the relation $\omega = 2\pi/P$. The quantity r_c is then the radius of the light cylinder.

Charged particles, as plasma, are emitted from the surface of the neutron star at various expelling potentials (Spitkovsky, 2005). If expelled with the maximum potential of the pulsar, then the ejecta can detach itself from the field lines within the light cylinder, and escape the system to infinity. Otherwise, for lower expelling potentials, a substantially large amount of ejected plasma gets trapped within the closed field lines defined by the light cylinder. Although the larger part of the ejecta stays within the magnetosphere, the smaller portion of escaping charged particles makes the magnetosphere to be partially filled. The particle kinetic-energy density in the magnetosphere is thus less than the magnetic-energy density. Although the field lines co-rotate with the pulsar the partial filling-up of the magnetosphere with plasma produces differential rotation in that some field lines do *not* co-rotate with the system, or rotates at different angular velocities than the pulsar (Spitkovsky, 2005). That is some zones do not rotate along while zones at different distances from the surface rotate with different velocities. These differential co-rotation leads to instabilities within the system — known as *diocotron instabilities*. In fluid dynamics, these instabilities are known to produce vortex structures.

Co-rotating charges only exist within the light cylinder. Even though in the region beyond the light cylinder co-rotating charge clouds ceases to exist (Goldreich & Julian, 1969), these is also not vacuum.

2.3.6 The Supernova Shockwave

NASA (2006) gives the progressive development of matter after a supernova explosion. The material expelled from the star's outer layers during the supernova explosion moves in all directions outwards with speeds commonly exceeding 10^3 km/s. These velocities are much larger then the velocity of sound in the medium, therefore a radially propagating shockwave is produced. This supersonic ejecta thrushes through the interstellar material or circumstellar medium, compressing and heating it up to temperatures above 10^6 K.

The heated ISM gets propelled away in a spherical shell at speeds slightly less than the initial thrusting shock speed. This shocked shell consists of the initial ambient interstellar matter and the stellar ejecta that has intruded it. The shockwave persistently sweeps up the ISM. The latter also grows in mass the further away the shock gets from the central pulsar. Therefore, the shockwave is subject to some dynamics as described below in terms of stages. These stages are characterized by observational properties of the system over time.

It is essential to note at this point that even though typically at earlier times the pulsar is located near the center of the SNR, it can have a velocity of $\sim$ 500 km/s in some direction. A motion that can over extensive time periods get the pulsar out of the SNR, leaving behind a "relic" PWN. Such a spatial pulsar velocity is attributed to asymmetry or irregularities that might have been present during the supernova explosion (Gaensler & Slane, 2006). It can take a spatially moving pulsar, at the speed quoted above, roughly 40 000 years to escape its supernova remnant shell. We need to note however that even if a pulsar has escaped its PWN, it will always be creating smaller PWN at its new location. This is simply due to its nature of powering the environment.

↪ The Shockwave in the Free-Expansion Phase

In the initial stages, the mass of the material swept up by the forward moving shock is very much less than the ejected stellar material. These is inevitable in the beginning because only the relatively close regions that surround the supernova are involved. The situation makes it fairly easy for the expansion to be rather smooth, hence the name *free-expansion.* The PWN therefore expands freely at supersonic speeds (Gaensler & Slane, 2006). The free-expansion phase may last for a few hundred years, as the swept up mass accumulates.

↪ The Shockwave in the Sedov-Taylor Phase

The shockwave enters the *Sedov-Taylor* phase when the swept up ambient material is about of the same mass as the ejecta which drives it outwards. As a result of the accumulated instellar mass, the shockwave will experience increased resistance and will eventually decelerate. The system will now develop multiple structures — a reverse shock is now observed (Gaensler & Slane, 2006). Figure 2.3 shows the schematic

layout of the system at this stage. The reverse shock, which is accountable for the deceleration of the ejecta, is a reaction by the ISM when heated and compressed. This evolutionary stage is also known as the *adiabatic* phase. The rate of expansion of the shock now becomes a function of the total involved ISM and the initial ejected mass.

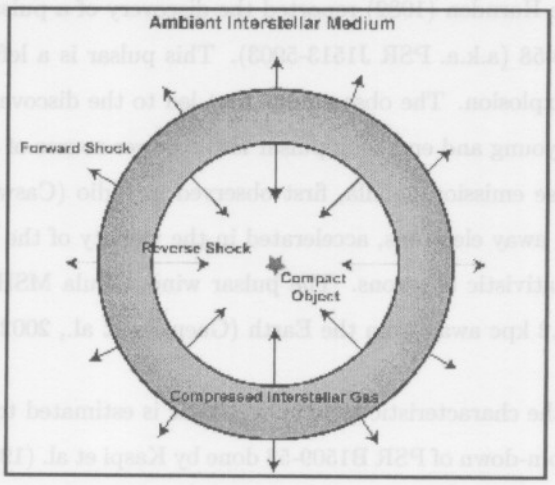

Figure 2.3: *A schematic view of the forward expanding shockwave and the resultant reverse shock exerted on the ejecta (NASA, 2006). The star in the center represents the pulsar position, if the explosion is perfectly symmetric — this may however not be the case in reality, resulting in an off-set of the pulsar position from the center of the SN.*

In the early stages, the reverse shock also moves outward trailing the forward shock. However, the reverse shock later moves in the opposite direction — moving inwards. Thus the reverse shock can in principle reach the center of the SNR, causing instabilities when it collides with the PWN.

↪ THE SHOCKWAVE IN THE RADIATIVE PHASE

The deceleration of the forward shockwave, due to the escalating amount of interstellar material in the way, continues resulting in a considerable decline of its temperature to $< 10^4$ K. Its thermal energy is transferred into radiation, hence the name *radiative phase.* Ultraviolet line emission takes place due to the recombination of electrons with carbon and oxygen ions. The radiative phase can last over thousands of years.

2.4 PSR B1509-58 & MSH 15-52

2.4.1 The History & the Parameters of the System

About 24 years ago Seward & Harnden (1982) reported the discovery of a pulsar, in X-rays, now known by its catalog name, PSR B1509-58 (a.k.a. PSR J1513-5903). This pulsar is a left over spinning neutron star of the associated supernova explosion. The observatory that led to the discovery of PSR B1509-58 was the Einstein space mission. This young and energetic pulsar is the power source of a surrounding diffuse nebula called MSH 15-52. The diffuse emission nebula, first observed in radio (Caswell et al., 1981), is reckoned to be generated by streaming away electrons, accelerated in the vicinity of the pulsar. A termination shock front is generated by this relativistic electrons. The pulsar wind nebula MSH 15-52 (a.k.a. G320.4-1.2) is located a distance of about 5.2 kpc away from the Earth (Gaensler et al., 2002).

By means of Equation 2.10, the characteristic age of this pulsar is estimated to about 1700 years (Gaensler et al., 2002). A study of the spin-down of PSR B1509-58 done by Kaspi et al. (1994) gives the spin parameters of the pulsar as shown in Table 2.1. The reference date of these parameters in MJD (Modified Julian Day) format is 48355.0000, which corresponds to April 9, 1991 on the Gregorian calendar. The position parameters are given as J2000 coordinates.

Parameter	**Value**
Right Ascension (RA)	$15^{h}\ 13^{m}\ 55.62^{s}$
Declination (DEC)	$-59^{\circ}\ 08^{m}\ 09.0^{s}$
Frequency (ν)	$6.6375697328\ s^{-1}$
1^{st} frequency derivative ($\dot{\nu}$)	$-6.7695374 \times 10^{-11}\ s^{-2}$
2^{nd} frequency derivative ($\ddot{\nu}$)	$1.9587 \times 10^{-21}\ s^{-3}$
3^{rd} frequency derivative ($\dddot{\nu}$)	$-1.02 \times 10^{-31}\ s^{-4}$
Braking index (n)	2.837
EPOCH (MJD)	48355.0000 [i.e. 9^{th} April 1991]
Age	1691 years

Table 2.1: *Location and spin-parameters of PSR B1509-58 as given by Kaspi et al. (1994).*

Although the discovery of this pulsar dates back a mere 24 years, the supernova remnant, MSH 15-52, it resides in has been known as far back as in 1961 as seen in the work quoted by Aharonian et al. (2005a). MSH 15-52 was initially observed as an non-thermal radio source. The morphology of the system was since

then perceived as being complex. This SNR is a composite system, with the central pulsar powering a PWN and a supernova remnant shell around it (Khélifi, 2005). An optical H_α nebula, RCW 89 consisting of filament-like structures, have also been seen in this association (Yatsu et al., 2006).

From X-ray studies, Gaensler et al. (2002) confirms a clear axis of symmetry associated with the overall system. As can be seen in Figure 2.5, the diffuse nebula extends along the northwest-southeast of the pulsar (marked with a dot). It is now accepted (see e.g. Gaensler et al., 2002) that this main axis of the nebula coincides with the pulsar spin axis.

2.4.2 Complexity of MSH 15-52

Some fundamental aspects of MSH 15-52 have not been resolved yet. That is, there are features and discrepancies that this source is associated with. These include the following aspects:

↪ The Age Discrepancy

Although the spin-down age of the PSR B1509-58 is estimated to be 1700 years, Gvaramadze (2001) suggested that the supernova remnant associated with the pulsar, MSH 15-52, should be about 20 000 years old. The latter age is deduced from the shape and general appearance of the SNR. These two time scales are one order of magnitude different for systems that are so closely related.

Gvaramadze (2001) gave explanations for the age discrepancy between SNR MSH 15-52 and PSR B1509-58. His argument is that the pulsar moves through an inhomogeneous ambient medium — at some occasions plunging through clumps of dense matter. Such dense clumps are reckoned to increase $\dot{\nu}$ temporarily. This inconsistency is regarded as the source of the underestimation of the pulsars characteristic spin-down age.

↪ Morphological Complexity

Gaensler et al. (2002) describe the SNR MSH 15-52 as a system with "complicated morphology". The object is described as having an unusual radio appearance, so much so that initially it was thought to consist of two or three SNRs (Gaensler et al., 2002) — a suggestion that was later nullified. It can be seen in Figure 2.4 (a Chandra X-ray Observatory image) that the complex nebula is aligned in a north-west south-east orientation. In addition, it can be seen that Figure 2.4 shows various features, with various densities and shapes.

The feature marked as **A**, in Figure 2.4, represents PSR B1509-58. Features marked **B** to **F** represent all shapes and sizes of prominent emission regions of the system. The optical emission region RCW 89 can be seen in the north-west region. This system does not have a simple morphology.

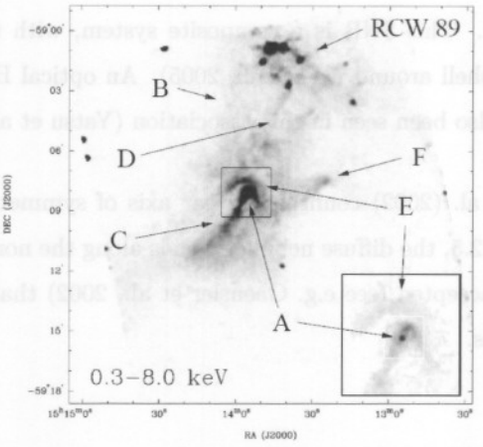

Figure 2.4: *An intricate Chandra X-ray image of MSH 15-52 as shown in Gaensler et al. (2002). The optical* H_α *nebula (RCW 89) can be seen in the northern region. The position of the pulsar B1509-58 is marked with an* **A**. *Other features marked with letters from* **B** *to* **F** *are regions with various densities and sizes.*

2.4.3 The Discoveries by H.E.S.S.

A survey in search of VHE γ-ray sources in the Galactic plane was carried out by H.E.S.S. since 2004. This survey explores the galactic longitude range $300° < \ell < 330°$ (Gallant, 2006). A total of 14 VHE sources were positively identified as VHE γ-ray sources. Of these sources some are already well-known sources while others are new discoveries. H.E.S.S.' observations revealed VHE γ-ray emission from 4 previously known sources and discovered 10 additional sources — a numerous list of discoveries.

The known sources that were seen by H.E.S.S. in VHE γ-rays are the Crab Nebula, SNR G0.9+0.1, SNR MSH 15-52, and the Vela SNR. These, as well as the newly discovered sources, are shown in Table 2.2. The list, compiled from Gallant (2006), gives the name of the extended source along with the associated central pulsar, if any.

↪ CRAB NEBULA

Since it is an exceptionally well-studied astronomical system, observations of the Crab Nebula is of utmost importance. Listed first in Table 2.2, H.E.S.S. observed the "standard candle" as a center-filled plerion with non-thermal emission (Gallant, 2006). The Crab nebula, located at a distance of about 2 kpc with an age of 950 years, was first seen in VHE energies in 1989 (Aharonian et al., 2006a). The central pulsar, the Crab pulsar, has a rotational period of 33 ms.

↪ SNR G0.9+0.1

A central pulsar has not been observed yet for this well-known composite system. It is revealed in Gallant

VHE γ-ray source	Associated pulsar	Status of the source
Crab Nebula	Crab pulsar (a.k.a. B 0531+21)	known before
SNR G0.9+0.1	none yet	known before
MSH 15-52	B 1509-58	known before
Vela SNR	Vela pulsar (a.k.a. B 0833-45)	known before
HESS J1420-607 *	J 1420-6048	discovered by H.E.S.S.
HESS J1418-609 *	none yet	discovered by H.E.S.S.
HESS J1825-137 †	B 1823-13	discovered by H.E.S.S.
HESS J1616-588 †	J 1617-5055	discovered by H.E.S.S.
HESS J1804-216 †	B 1800-21	discovered by H.E.S.S.
HESS J1303-631 †	J 1301-6305	discovered by H.E.S.S.
HESS J1702-420 †	J 1702-4128	discovered by H.E.S.S.
HESS J1813-178	none yet	discovered by H.E.S.S.
HESS J1834-087	none yet	discovered by H.E.S.S.
HESS J1634-472	none yet	discovered by H.E.S.S.

Table 2.2: *The list of more than dozen VHE γ-ray sources discovered by H.E.S.S. Some of this SNRs are associated with already known pulsars. The two sources marked with * are located in the Kookaburra supernova remnant. Sources marked with † are newly discovered sources possibly associated with the respective pulsars. This table was created from Gallant (2006).*

(2006) that a shell of emission encloses a plerion, and that the plerion seems to be the dominant γ-ray emitter. It was the first time that H.E.S.S. detected VHE γ-rays from this source — in fact it is one of the faintest sources detected at TeV energies (Aharonian et al., 2005b).

↪ MSH 15-52

The H.E.S.S. discovery of MSH 15-52 marks the first ever PWN discovered in VHE γ-ray emission. MSH 15-52 is a composite system hosting the pulsar B 1509-58. The nature of the γ-ray emission from this region is the topic of this work. The discovery of H.E.S.S. regarding MSH 15-52 is discussed later in broader detail.

↪ Vela SNR

The Vela supernova remnant is another well-known system across the electromagnetic spectrum, of which H.E.S.S observed its inner region within 2° of the associated pulsar B0833-45. These observations revealed an extended source of VHE γ-ray emission to the south of the pulsar — the pulsar is not central in the SNR (Gallant, 2006). H.E.S.S.' results from Vela observations shows the first ever clear peak in the spectral energy distribution from a VHE γ-ray region (Aharonian et al., 2006b).

↪ Sources in the Kookaburra SNR

The Kookaburra[2] region is a large circular thermal shell located around the galactic longitude of $\ell \approx 313°$

[2]The Kookaburra region is named after an Australian bird (see e.g. Aharonian et al., 2006c)

(Aharonian et al., 2006c). H.E.S.S. discovered VHE γ-ray sources coinciding with the two radio 'wings' in the north-east and south-west regions of this source. The two 'wings' are, HESS J1420-607 in the north-eastern, and the narrower HESS J1418-609 in the south-western regions of the Kookaburra complex (see Aharonian et al. (2006c) & Gallant (2006)). Although the latter is not yet associated with a pulsar, HESS J1420-607 is believed to be powered by pulsar J 1420-6048.

↪ POSSIBLE PWN-PSR ASSOCIATIONS

Apart from the new source in the Kookaburra region HESS J1420-607, H.E.S.S.S. discovered five more extended VHE energy emitters that are possibly associated with some pulsars, of which most of the pulsars are not located at the centers of the extended nebulae — suggesting that these are relatively old PWNe (Gallant, 2006). These associations are marked with † in Table 2.2.

↪ SOURCES WITH NO DETECTED ASSOCIATIONS

In addition to the already known supernova remnant G0.9+0.1 and the newly discovered HESS J1418-609 in the Kookaburra source, H.E.S.S. discovered three more extended VHE γ-ray sources that are not at present associated with pulsars. These are listed in Table 2.2 as HESS J1813-178, HESS J1834-087 and HESS J1634-472. It is reckoned that deeper observations may explore the possibility of pulsar associations in the future (Gallant, 2006).

Back to the H.E.S.S. discovery of VHE γ-ray emission from MSH 15-52. Prior to the Galactic plane survey mentioned earlier, H.E.S.S. observed MSH 15-52 in a stereoscopic mode between March and June 2004, for a total live time of 22.1 hours (see Aharonian et al., 2005a). This total live time is obtained after selecting data taken during optimum weather and triggering system conditions. The excess of events from the direction of the source was recorded — the so-called DC excess[3]. H.E.S.S. produced the following excess map, Figure 2.5, of the composite system of MSH 15-52.

It is very important to note that Figure 2.5 is the first such resolved image of an extended pulsar wind nebula in VHE γ-ray astronomy. The image also fits previously obtained X-ray images very well, as we can see the agreement between the white contour lines (representing the X-ray count rate measured by ROSAT (RÖentgen SATellite)). Figure 2.5 clearly shows the same morphology as seen in Figure 2.4 — confirming the identity of the source.

As for the size of MSH 15-52, radio studies by Caswell et al. (1981) revealed this source as a roughly circular region with an angular diameter of 29 arcmin. The elongated PWN seen in Figure 2.5 has a $\sim$ 6 arcmin semi-major axis and a semi-minor axis of $\sim$ 2 arcmin. Aharonian et al. (2005a) also found that PSR B1509-58 has a larger energy conversion efficiency than the well known Crab pulsar. With the energy conversion being defined as in Equation 2.6, PSR B1509-58 has a energy conversion of $\sim$ 0.6% while the Crab's is $\sim$ 0.02%.

[3]A emission source can be detected via one of the following methods: The excess events from the direction of the source can be recorded, or one can establish periodicity in the pulse arrival times from the source direction (Lewis, 1989).

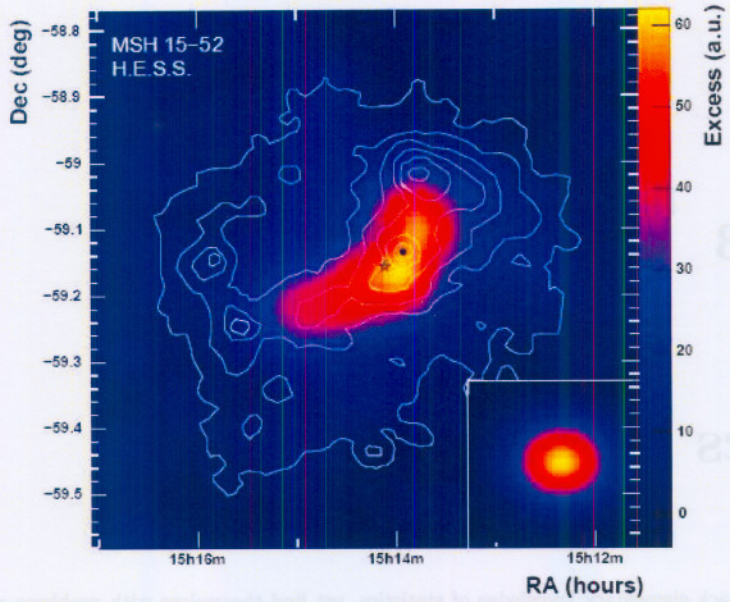

Figure 2.5: *The VHE γ-ray excess map of MSH 15-52 as indicated by Aharonian et al. (2005a). The contour lines were produced from X-ray observations of ROSAT (RÖntgen SATellite), while the gray-scale represents the excess map from H.E.S.S. The dot represents the pulsar positions, whereas the star denotes the excess centroid.*

Using the commonly assumed moment of inertia of 10^{38} kg m^2 (Gaensler & Slane, 2006), we deduce the rate of change of energy for the pulsar B1509-58 as 1.8×10^{37} erg s^{-1}, from Equation 2.4 and timing parameters in Table 2.1. The equatorial surface magnetic field of this pulsar can similarly be estimated using Equation 2.15 as $\sim 1.5 \times 10^9$ T.

Every month since its full operations commenced, H.E.S.S. features a so-called *source of the month* on its official website. The selected source is a TeV γ-ray source observed with the H.E.S.S. telescope array. The significance of studying MSH 15-52 was highlighted when it was selected as the source of the month for June 2005, under the heading (see H.E.S.S. website):

"MSH 15-52 - A PULSAR WIND NEBULA WITH A JET"

As MSH 15-52 is one of the most prominent and well-known extended sources discovered by H.E.S.S. in γ-rays, we selected it, to test the possibility of a pulsed signal being propagated into the PWN.

Chapter 3

Statistics in γ-ray Astronomy

"Physicists often lack elementary knowledge of statistics, yet find themselves with problems requiring advanced methods — if adequate methods at all exist." — Eadie et al. (1971)

3.1 Introduction

WE now briefly deal with the subject of statistics. We have to do this now, simply because data analysis of γ-ray data are largely dependent on statistical methods. Lindley (2000) defines statistics as the study of uncertainty, and that the statistician is there to assist workers from other fields, 'clients', with handling uncertainty in their work. Uncertainty, in statistics, is measured by probability.

In what follows we would like to introduce to the reader the basic concepts, from statistics, that we employ for the data analyses carried out in this work. The underlying principle pertains the use of *hypothesis testing* techniques of statistics for analyzing γ-ray data. The fundamental statistical terms and concepts that we are concerned with is introduced, as we explain the process of data analyses. The data that we deal with basically consist of timing entries, the so-called photon *times-of-arrivals* (ToAs).

3.2 Circular Data

Timing data can be viewed as *circular data* as can be seen in ,for example, Mardia & Jupp (1999). Elements of circular data can be regarded as points on the circumference of a circle of unit radius. Each such data

point can be specified by a vector pointing from the center of the circle to the location of the point on the circumference, as shown in Figure 3.1. Therefore, each such entry can be described by a direction (i.e. by a unit vector) — hence the alternative name *directional data.* Figure 3.1 shows how directional data can be represented on a circle. Circular data can be timing records of γ ray pulses, directions of bird migration, wind directions, etc.

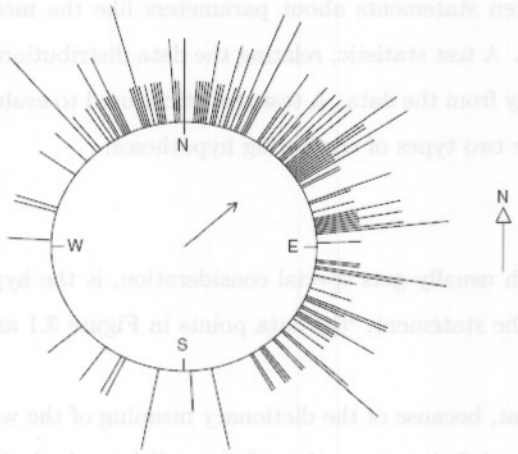

Figure 3.1: *A typical schematic representation of directional or circular data as shown by Cox (2001). the arrow shown denotes the dominant direction of the points on the circle as being north-east. The hypothetical data which produced this result, is non-uniformly distributed on the circle.*

From Figure 3.1, one can see that the north-east direction is dominant for that data. That is the mean direction points north-easterly. So one could also say (assuming east corresponds to 0 radians) that the preferred angle is $\frac{\pi}{4}$ radians. However, if the distribution of the directions on the circle in Figure 3.1 had been uniform, then we would have no preferred angle.

Circular data is analyzed by checking the uniformity of the data on a circle. This is customarily done by 'suggesting' a preferred direction (non-uniformity) and checking for its validity via the statistical process of *hypothesis testing.*

3.3 Hypotheses Testing

In statistical inference methods, hypothesis testing is a technique whereby a certain 'claim' is made about some data and then putting it under 'scrutiny'. The claim takes the form of an unproved statement made,

based on some sound presupposed arguments, regarding the data set — and is called *the hypothesis*. The scrutiny takes the form of a mathematical check on some values computed from the data set — and is referred to as *the test*. For example, if we make a hypothesis that the data producing Figure 3.1 is uniformly distributed, and we go on to show that such a claim is not satisfactory, then we have just performed hypotheses testing.

Generally, hypotheses are often statements about parameters like the mean, the variance or some other "test statistic" about the data. A test statistic, relating the data distribution to the hypothesis, is a quantity calculated in some sensible way from the data. A test statistic is used to evaluate the validity of a hypothesis. In a hypothesis test, there are two types of competing hypotheses.

↪ THE NULL HYPOTHESIS

The first hypothesis, which usually gets special consideration, is the hypothesis that is tested — called the *null* hypothesis H_0. The statement, "the data points in Figure 3.1 are uniformly distributed", would be a typical H_0.

It is interesting to note that, because of the dictionary meaning of the word 'null', as *invalid* or *insignificant*, some people have an inferior perception of the null hypothesis (Greenwald, 1975). However, in statistics H_0 refers to the absence of some association between certain variables.

↪ THE ALTERNATIVE HYPOTHESIS

The *alternative* hypothesis H_A is the claim that stands awaiting to be accepted, when the null hypothesis gets rejected. This is usually *the* idea why the statistical test has been set up — the hypothesis that the researcher wants to prove. In our example of Figure 3.1, H_A could be stated as "the vectors in Figure 3.1 are generally oriented in a north-east direction".

The general idea is as follows: State a claim and prove it wrong. It is in analogy to the situation in most justice systems:

> "The suspect is innocent (H_0) until proven guilty (H_A) beyond any reasonable doubt"

Guttman (1977) refers to H_0 as the 'incumbent' hypothesis and H_A as the 'challenging' hypothesis. The incumbent holds until overwhelming evidence against it is shown.

3.4 Statistical Inference

Statistical inference refers to the decision making part of a statistical test. That is the interpretation of the test results. The procedure is that the two hypotheses are first established. Then a suitable statistical test is selected or constructed, followed by the computation of the relevant test statistic. The so obtained test statistic is then used to compute the so-called 'p-value' or 'p-level', which in simplest terms is a probability of making an error in a statistical test. The observed p-value is then compared to an already set standard level. If the observed p-level is smaller than the standard p-level, then the results can be deemed as statistically significant. This standard level is also known as the *significance level.* In most social science research, the significance level is set as 0.05 (or 5%). Since this work requires a very high accuracy, as we would like to determine a pulsar period at millisecond accuracy, a rigorous significance level is required — which we will set as 10^{-4}.

Depending on the value of the observed test statistic in relation to the required significance level, the null hypothesis can either be accepted or rejected. The observed data-dependent p-level should be less than 10^{-4} to ensure the rejection of the null hypothesis, *in favour of the alternative hypothesis* H_A.

For some statistical tests, like the χ^2-test, the significance levels are given by statistical contingency tables, where the associated *degrees of freedom*[1] are also considered. For electronic and interactive χ^2 calculators see e.g. USC (2006).

Upon completion of a statistical test, a decision has to be taken regarding the stated null hypothesis. This process known as the statistical inference, constitutes either rejecting or accepting of the null hypothesis. The decision taken can lead to four basic outcomes as shown below:

↪ TYPE I ERROR

Rejecting the null hypothesis H_0, while it is actually true, amounts to a *Type I error* (see e.g. Berger et al., 1997). The probability of wrongly rejecting H_0 is denoted by α — hence it is also known as the α-error.

↪ TYPE II ERROR

On the contrary, accepting a false null hypothesis H_0, is regarded as having committed a *Type II error.* Also known as the β-error, its probability is β as seen in e.g. Berger et al. (1997).

Hypothesis testing and the inference from it can result in a total of four outcomes — as shown in the next

[1]The concept of degrees of freedom (as employed here) assumes the perspective of statisticians — referring to the number of unrestricted variables given estimates of a parameter — as opposed to the physics definitions as in the case of thermodynamic variables (Wikipedia, 2006b).

diagram. The outcomes are the ones framed in oval boxes.

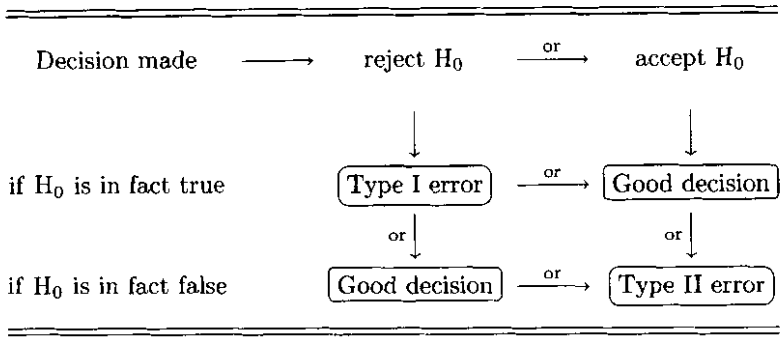

Two of the outcomes are erroneous, and the other two are correct. A successful test and inference should strive to make any one of the two "good decisions", and reduce the risks of reaching the erroneous decisions. However, it is so that reducing the risk of falsely rejecting the null hypothesis, increases the risk of falsely accepting it. Hence, there is an inverse relation between Type I error and Type II errors. Even so, a Type I error is considered more serious than a Type II error, therefore the test is constructed so as to minimize α.

With these definitions of the possible errors, we can now formally revisit the concept of the significance level. The significance level is the probability of making a Type I error. Therefore, by setting our standard significance level very small ($\sim 10^{-4}$), we protect H_0 from being falsely rejected. Therefore, values of the observed p-value that are smaller than the significance level suggest that H_0 is unlikely to be true — a situation which favours the alternative hypothesis H_A.

Note, that not being able to reject H_0 does not imply that it is true — there is simply not enough evidence against it.

Values for which the null hypothesis is rejected, are said to be in the *critical region.* By making the significance level very small, we make the critical region smaller. The smaller the critical region, the smaller the probability of making a Type I error.

3.5 The Power of a Test

The *power* of a statistical hypothesis test determines the ability of the test to reject H_0 when it is false. In other words, the power of a test measures how good the test is in making *the right* decisions. The power of a test is given by $1 - \beta$, and as such, it is related to the probability of not committing a Type II error. In

terms of the alternative hypothesis, the power of the test is the probability of accepting the 'challenging' H_A hypothesis when it is true.

It is reported (see Johnstone et al., 1986) that in its initial introduction the concept of 'power' (developed by Jerzy Newman and Pearson) was in rivalry with a concept of 'sensitivity' (introduced by Ronald Fisher). Sensitivity was introduced to measure the ability of the test to detect some departures from the null hypothesis. Sensitivity manifests itself via the p-level, thus today both of these concepts are incorporated.

3.6 H_0 and H_A in γ-ray Astronomy

Pulsars and SNRs emit γ-rays as a results of physical processes such as inverse Compton scattering, curvature (synchrotron) radiation, bremsstrahlung and pair production, as discussed in § 2.2.3. The Earth's atmosphere interacts with the incident γ-ray, leading to the arrival of photons on the Earth's surface in the form of Cherenkov light. Pulsar timing constitutes the recording of photon arrival times. We will refer to such data as γ-ray data. The periodicity of the emission can then be investigated by performing statistical analysis of the data.

As we have now (hopefully) put the basic statistics required in place, we proceed with its application to the statistical analysis of γ-ray data. The approach is to give meaning to statistical concepts like significance level and p-level when used in the analysis of γ-ray data.

First we need to make our intention very clear — we are searching for pulsed signals. We do this search by means of hypothesis testing techniques, which requires statements for the two hypotheses as discussed earlier. In γ-ray periodicity analyses, these hypotheses looks as follows.

↪ H_0 FOR γ-RAY DATA

In general, the null hypothesis should assume that there are no particular relations between variables. This is equivalent in assuming that the distribution of photon arrival times are not prescribed by some variables through some kind of a distribution model. Hence, the null hypothesis H_0 states that:

> **"The photon arrival times are uniformly distributed, hence there is no periodicity in the γ-ray emission from MSH 15-52"**

↪ H_A FOR γ-RAY DATA

The alternative hypothesis should challenge the null hypothesis. Indeed, this is the primary idea that we investigate. We are searching for the periodicity, hence the alternative hypothesis H_A presumes that:

"The photon arrival times are non-uniformly distributed, hence γ-ray emission from MSH 15-52 is pulsed"

Pulsar B1509-58 is a periodic radio emitter. We would like to investigate if a VHE γ-ray periodicity can be observed in data taken from the associated nebula, MSH 15-52. We set the null hypothesis as a negation statement to this sensible argument, and then we try to disprove it. The task is to get enough evidence (in the form of small p-values) against the null hypothesis, in order to claim the existence of pulsed signals in the data.

Concepts like the significance level and the computed p-level have specific meanings in the analysis of γ-ray data. The significance level, set as $\sim 10^{-4}$, is called the "detection threshold" (see de Jager, 1987). It should some however be noted that some researchers would make detection threshold even lower to $\sim 10^{-6}$ depending on the involved degrees of freedom. For observed p-values $< 10^{-4}$, we have some evidence in favour of the alternative hypothesis — detection of a pulsed signal. At a later stage, we will introduce the concept of 'significance', which should not be confused with the "significance level". To avoid ambiguity, we will refer to the "significance level" as the detection threshold.

We note that de Jager (1987) refers to the data-dependent p-value as the "probability of uniformity", and as the name suggest large values of it favours the null hypothesis. The concept of significance mentioned in the previous paragraph, is obtained directly from the p-level, as will be shown at the appropriate stage.

There are numerous types of tests that are employed by γ-ray data analyst, when searching for pulsed signals. Various such test where studied by for example de Jager (1987) to determine their strength and weaknesses in various situation. For all these tests, the underlying concept is the idea of testing circular data for its uniformity on the circle.

3.7 Test for Uniformity

Each datum of the obtained timing data series can be represented by a point on the circumference of a circle. In our case, we would like to test for evidence of pulsed γ-ray emission in the data, at and near the radio period. To do this, we inspect the distribution of the points on the circle. Data points on a circle will not be uniformly distributed on the circumference if there is some periodicity. Therefore, the significance of the signal is assessed by simply checking if the data are uniformly distributed on the circle.

3.7.1 Folding ToAs at Period

Each ToA is converted into a phase. This transformation process requires the spin parameters of the pulsar. These parameters include, the pulsar frequency ν and its time derivatives or alternatively the pulsar period P and its derivatives. Each ToA is then represented by a phase value. If $t_i = \{t_1, t_2, t_3, \ldots, t_n\}$ are the photon arrival times (for a data set of n ToAs), then the corresponding phases $\bar{\theta}_i$ are obtained from the following Taylor expansion:

$$\begin{aligned} \bar{\theta}_i &= \nu + \dot{\nu}\, t_i + \frac{1}{2}\ddot{\nu}\, t_i + \frac{1}{6}\dddot{\nu}\, t_i + \cdots \\ &= \frac{1}{P} - \left(\frac{\dot{P}}{P^2}\right) t_i + \left(\frac{\dot{P}^2}{P^3} - \frac{\ddot{P}}{2P^2}\right) t_i^2 + \left(\frac{\dot{P}\ddot{P}}{P^3} - \frac{\dot{P}^3}{P^4} - \frac{\dddot{P}}{6P^2}\right) t_i^3 + \cdots \end{aligned} \tag{3.1}$$

The test is preceded by 'folding' of the phases. Folding is a technique by which continuous, strictly increasing, values are projected onto a desired interval. The folded phases $\theta_i \in [0, 2\pi]$ are obtained by doing

$$\theta_i = 2\pi \left(\bar{\theta}_i - \text{integer}(\bar{\theta}_i)\right) \tag{3.2}$$

where 'integer($\bar{\theta}_i$)' is the integer part of $\bar{\theta}_i$. These manipulations leaves us with phases that are folded at the radio period of the pulsar. All phases have been mapped onto one pulsar period, and normalized to the interval from 0 to 2π. These phases are then tested for uniformity on the circle.

The test is done at and near the radio period of the pulsar. To get contemporary pulsar parameters, the known radio ephemerides needs to be extrapolated to the time of observation (Oña-Wilhelmi & de Jager, 2002). If the pulsar period from the ephemeris is at some epoch is P_0 (corresponding to ν_0), then the expected period P_{ex} and frequency ν_{ex} after time Δt is given by

$$\begin{aligned} \nu_{ex} &= \nu_0 + \dot{\nu}\, \Delta t \\ P_{ex} &= P_0 + \dot{P}\, \Delta t \end{aligned} \tag{3.3}$$

Note that Δt is the time elapsed between the ephemerides' epoch date and the observation time. In Equations 3.3, $\dot{\nu} < 0$ while $\dot{P} > 0$ ensuring that the pulsar period increases gradually with time, while the frequency decreases in the same fashion — as common sense permits.

3.7.2 The IFS

We then test for periodicity at and near the extrapolated radio period. To test for periodicity near the expected period calls for the concept known as the *independent Fourier spacing* (IFS). An IFS is the magnitude by which independent sequential period values are spaced. If T is the total duration of the observation, then the space between two independent periods P_i and P_{i-1} can be seen in e.g. de Jager (1987) as

$$P_i - P_{i-1} = \frac{{P_{i-1}}^2}{T + P_{i-1}}$$

The IFS is a concept from Fourier analyses which ensures that one search for periodicity at the appropriate intervals. It thus does ascertains that a possible frequency embedded in signal-like data is not missed. We adopt the IFS as

$$\begin{aligned} IFS &= \frac{P_0^2}{T + P_0} \\ &\approx \frac{P_0^2}{T} \end{aligned} \tag{3.4}$$

where the approximation in the second part is encouraged by the fact that pulsar periods are negligible compared to the length of a typical observation. Even more, it is sufficient to approximate the IFS as simply

$$IFS \approx \frac{1}{T} \tag{3.5}$$

The last two equations may look dimensionally inconsistent — this is not so as Equation 3.4 gives the units of IFS as seconds, while Equation 3.4 only gives the approximated magnitude of the IFS. When searching for periodicity, the IFS is used to obtain a set of test periods around the expected frequency (or period). The set of test frequencies were obtained by computing

$$\nu_{ex_{i+1}} = \nu_{ex_i} - k\,\frac{i}{T} \tag{3.6}$$

where i are integers in the closed interval [1, 10]. However, by letting $i \in [-10, 10] \subset \mathbb{Z}$, we get a set of test frequencies[2] above and below the expected radio period. The test period range so obtained, constitutes 3 IFS on either side of the expected radio period (where IFS $\sim 10^{-4}$ s). In order to get 10 IFS on either side of the radio period, we let $i \in [-30, 30]$. In both cases, one IFS contains three test periods.

[2]Take note that $i = 0$, places the test frequency at exactly the initial test frequency — that is at the expected radio frequency ν_{ex}.

The constant k sets the fraction of IFS used — such that $k = 1$ represents the use of 1 independent Fourier spacing. In this work, we let $k = 1/3$.

3.8 The Rayleigh Test

Statisticians reckon that the Rayleigh test is amongst the most basic tests for uniformity on a circle (de Jager, 1987). This test for uniformity is named in honour of Lord Rayleigh[3] (1842-1919, born John William Strutt).

3.8.1 The Probability Density Function

The Rayleigh test investigates the distribution of the phases on a circle by means of hypothesis testing methods. According to Mardia & Jupp (1999), one important non-uniform distribution on the circle is the *von Mises distribution*, defined by the unimodal probability density function

$$f(\theta) = \frac{e^{\kappa}\cos(\theta - \mu)}{2\pi I_0(\kappa)} \tag{3.7}$$

In Equation 3.7 the quantity μ stands for the *mean direction* — denoting the position of the peak on the circle. The quantity κ is the *concentration parameter* — describing the width of the peak. The function $I_0(\kappa)$ is the *modified Bessel function of the first kind* (Mardia & Jupp, 1999), which looks like

$$I_0(\kappa) = \frac{1}{2\pi}\int_0^{2\pi} e^{\kappa\cos\theta} d\theta \tag{3.8}$$

For a uniform distribution, the concentration parameter vanishes. Therefore, inserting $\kappa = 0$ in Equations 3.7 and 3.8 gives $f(\theta) = \frac{1}{2\pi}$. A non-uniform distribution will take the form as described by Equation 3.7 with some non-zero κ, in fact (de Jager, 1987) quotes the resulting non-uniform probability distribution function as

$$f(\theta) \approx \frac{1 + \kappa\cos(\theta - \mu)}{2\pi} \tag{3.9}$$

At this stage we van state the two hypotheses, in terms of the probability distribution function $f(\theta)$ as follows:

[3] A Physics Noble Prize Laureate in 1904. In 1873, this British physicist inherited the Barony of Rayleigh, as the 3rd Baron, after his fathers death.

↪ The null hypothesis in terms of $f(\theta)$
H_0: $\kappa = 0$, so that $f(\theta) = \frac{1}{2\pi}$

↪ The alternative hypothesis in terms of $f(\theta)$
H_A: $\kappa > 0$, so that $f(\theta) = \frac{1+\kappa\cos(\theta-\mu)}{2\pi}$

3.8.2 Rayleigh Test Parameters

As mentioned earlier, each datum in circular data can also be viewed as a vector drawn from the center of a circle to the circumference in some direction determined by the value of the datum. That is, the phases can be regarded as a set of directional data. With this line of thinking, we can write down a horizontal and vertical component for each phase. For a set of n events, the mean components (or trigonometric moments) will be $\frac{1}{n}\sum_{i=1}^{n}\cos\theta_i$ and $\frac{1}{n}\sum_{i=1}^{n}\sin\theta_i$. From these mean values we can construct the mean direction as

$$\bar{R}^2 = \left[\left(\frac{1}{n}\sum_{i=1}^{n}\cos\theta_i\right)^2 + \left(\frac{1}{n}\sum_{i=1}^{n}\sin\theta_i\right)^2\right] \tag{3.10}$$

The value $2n\bar{R}^2$, called the *Rayleigh statistic* $\mathcal{R}$ obeys a χ^2 distribution with two degrees of freedom (see e.g. Brazier, 1994). The Rayleigh statistic thus looks like

$$\mathcal{R} = \frac{2}{n}\left[\left(\sum_{i=1}^{n}\cos\theta_i\right)^2 + \left(\sum_{i=1}^{n}\sin\theta_i\right)^2\right] \tag{3.11}$$

The probability of correctly rejecting the null hypothesis, in favour of the alternative hypothesis, simply called the power of the Rayleigh test, is given by $n\bar{R}^2$, i.e.

$$\begin{aligned} \textit{Rayleigh power} &= \frac{1}{2}\mathcal{R} \\ &= \frac{1}{n}\left[\left(\sum_{i=1}^{n}\cos\theta_i\right)^2 + \left(\sum_{i=1}^{n}\sin\theta_i\right)^2\right] \end{aligned} \tag{3.12}$$

The observed p-value is obtained from the formula

$$\textit{p-level} = e^{-n\bar{R}^2}, \tag{3.13}$$

which in turn gives the observed significance as

$$\begin{aligned} significance &= -\log_{10}(p\text{-}level) \\ &= 0.43\, n\, \bar{R}^2 \end{aligned} \tag{3.14}$$

Rejection of the null hypothesis small values of the p-level or by large values of the significance, with respect to the detection threshold of 10^{-4}.

Putting all these together, one should be able to see that the observed p-value is inversely proportional to the Rayleigh power. As an example, see a typical outcome of a Rayleigh test shown graphically in Figure 3.2. Therefore, a very small observed p-value, which will indicate a periodicity, is equivalent to obtaining a large Rayleigh power. There is a linear relationship between the Rayleigh power and the observed significance, the latter being slightly less than half of the former (this can also be seen in the example shown in Figure 3.2).

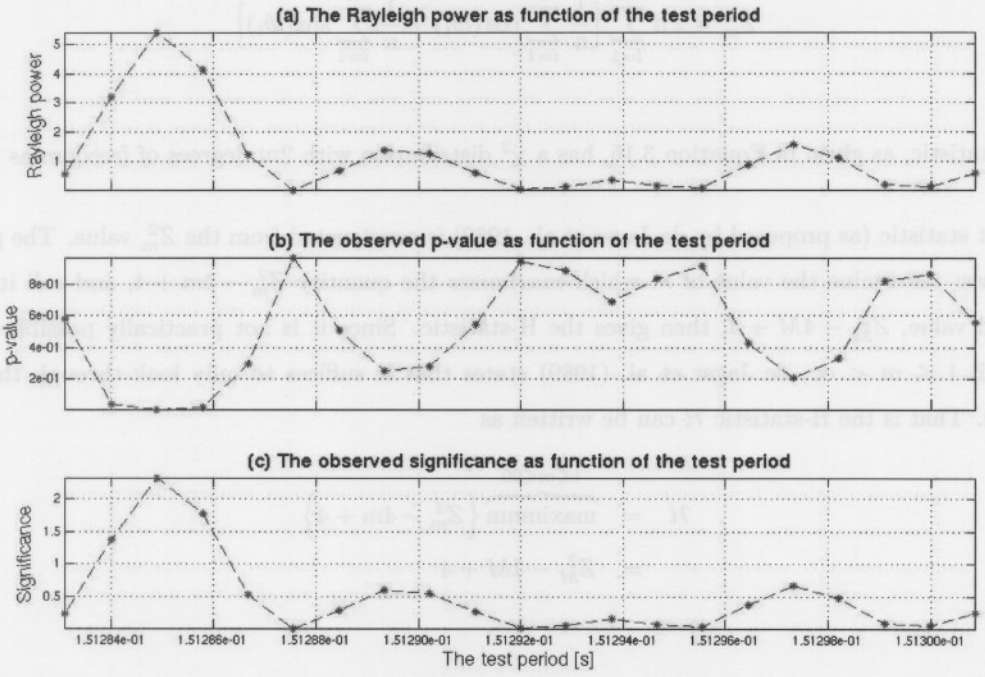

Figure 3.2: *Graphic view of the relationships among (a) the Rayleigh power, (b) the p-value and (c) the significance obtained from a Rayleigh test. Note that the Rayleigh power and the p-value have an inverse relationship, while the significance is almost half of the Raleigh power. The same horizontal axis holds for all three panels.*

3.9 The H-test

The H-test was proposed by de Jager et al. (1989) as a powerful test in the event that the signals are weak and the associated *light curve* is also not known a priori. The light curve is a plot of the intensity of the observed electromagnetic radiation as a function of time.

The H-test is based on the idea of testing the power in various numbers of *frequency harmonics.* A harmonic frequency is an integer multiple of some fundamental frequency f, such that $2f$ is the second harmonic, $3f$ is the third harmonic etc. The fundamental harmonic f, is thus the first harmonic. In principle, a signal can have infinitely many harmonic frequencies (or simply harmonics). The type of wave form determines the amount of energy contained in various harmonics. In these case, the trigonometric moments, for say l harmonics, become $\frac{1}{n}\sum_{i=1}^{n}\cos(l\theta_i)$ and $\frac{1}{n}\sum_{i=1}^{n}\sin(l\theta_i)$.

With these, we now define a statistic known as the Z_m^2 statistic as

$$Z_m^2 = 2\,n\sum_{l=1}^{m}\left[\frac{1}{n}\sum_{i=1}^{n}\cos(l\theta_i)+\frac{1}{n}\sum_{i=1}^{n}\sin(l\theta_i)\right] \tag{3.15}$$

The Z_m^2 statistic, as given in Equation 3.15, has a χ^2 distribution with $2m$ degrees of freedom as $n \to \infty$.

The H-test statistic (as proposed by de Jager et al., 1989) is constructed from the Z_m^2 value. The procedure is as follows: determine the value of m which *maximizes* the quantity $Z_m^2 - 4m + 4$, and call it M. The maximized value, $Z_M^2 - 4M + 4$, then gives the H-statistic. Since it is not practically possible to search through all $1 \leqslant m < \infty$, de Jager et al. (1989) states that it suffices to only look through the first 20 harmonics. That is the H-statistic $\mathcal{H}$ can be written as

$$\begin{aligned}\mathcal{H} &= \overbrace{\text{maximum}}^{1\leqslant m\leqslant 20}\left\{Z_m^2 - 4m + 4\right\} \\ &= Z_M^2 - 4M + 4\end{aligned} \tag{3.16}$$

The hypothesis test procedure would now be as follows: Obtain the H-statistic $\mathcal{H}$, then use the obtained H-statistic and the associated degrees of freedom to compute an observed p-value. Now compare the observed p-value with the corresponding probability given in standard statistical contingency tables of a χ^2-distribution.

Note that for $m = 1$, we have $Z_m^2 = Z_1^2$. That is, *the Rayleigh test is a special case of the H-test.* In fact, the Rayleigh test checks for the power in the first harmonic while the H-test checks for the power in the first 20

harmonics. That is to say, the Rayleigh statistic $\mathcal{R}$, is constructed from the first harmonic, such that

$$\mathcal{R} = 2\,n\,Z_1^2$$

3.10 Eadie Combination

It is possible that segments of data may produce results that are not statistically significant enough, while these segments may show significant results upon combination. This is to say that it is possible that individual observations that shows no detectable pulsed signal at a certain test period, can in fact show otherwise if combined.

A special type of manner in which observed p-values can be combined is given by Eadie et al. (1971). This combinatory method that checks if individually undetectable signals combine to give a detectale signal will hereafter (in this work) be referred to as "the Eadie combination".

If the number of p-values p_i obtained for a test period from different observations are k, then the Eadie-combined value Z is given by (see Eadie et al. (1971), Buccheri et al. (1983) or de Jager (1987))

$$Z = -2 \ln \prod_{i=1}^{k} p_i \tag{3.17}$$

The quantity Z also has a χ^2_{2k}-distribution function, with $2k$ degrees of freedom, and should therefore give the corresponding probability of chance occurrence as given in contingency tables of statistics (see e.g. USC, 2006). This chance probability (or the 'new' p-value) then gives the compound significance through Equation 3.14. Thus for example, for $Z = 37.79$ the chance probability, as given by USC (2006), is 0.8002 with 46 degrees of freedom. These implies a significance of $-\log_{10}(\textit{p-level}) = 0.097$.

A large significance so obtained, implies greater evidence against the null hypothesis in favour of the alternative hypothesis.

3.11 Other Tests

There are numerous other statistical test that are available for analysis of timing data. However, different test have different abilities in terms of their power for different types of data. With the phrase 'types of

data', we refer to characteristics such as the signal strength, pulse width, the light curve and the number of peaks in a pulse.

A outline of the various statistical tests at disposal for astronomers to utilize, and their strengths and weaknesses can be seen in de Jager (1987). For the analysis of data presumed to be periodic, we have the Rayleigh test as a *parametric* likelihood ratio test. A parametric test makes some assumptions on the values (like the concentration parameter) defining the probability density function.

Non-parametric tests includes, the Pearson's test, the Z_m^2 test, the Kuiper's tests, Watson's tests, and the Protheroe's test. These are tests for which no assumptions of the underlying probability density function is made. These tests have their own advantages, e.g. Pearson's test is quite powerful in detecting narrow peaks. For large samples ($n > 100$), Protheroe's and Watson's tests requires lengthly computer time as they require n^2 computational steps (de Jager, 1987). We also note that, in his work using Kuiper's test (a variant of Kolmogorov-Smirnov's test), Paltani (2004) says the following about Kuiper's test:

> `Like Rayleigh's test, it uses the individual photon arrival times, and is therefore well suited to the analysis of faint sources.`

The Rayleigh test has been seen as being very useful for broad peaks, and for cases where the light curve is not known a priori (de Jager, 1987).

We used the Rayleigh tests based on the fact that it is the *universally most powerful* (UMP) test (Mardia & Jupp, 1999), such that it can detect a pulsed signal, if any, for all types of light curves. It is very sensitive to sinusoidal curves, and can detect pulsed signals in non-sinusoidal light curve with low significance. For this reason the Rayleigh test is very popular in astronomical data analysis. The H-test is described earlier, that we used, is an 'extension' of the Rayleigh test to more harmonics.

Chapter 4

Data Preparation

> "In the study of a point-like source, the γ-ray selection criteria based on shower shape must be complemented by a cut on the angle θ between the reconstructed direction and that of the source" — Lemoine-Goumard et al. (2006)

4.1 Introduction

THE 'cleanliness' of the data is a primary concern for data analysts. Before performing any statistical analysis one has to ensure that the data is 'clean'. With the word clean here, we refer to the refinement of the data until it reaches a state of readiness for meaningful statistical analysis to be performed. As used here, data cleansing has a very broad meaning. Cleaning could imply, the act of throwing out unwanted components, transforming into desired formats or reference frames, or doing corrections of some sort to the data (if needed), etc.

Cherenkov telescopes does not only detect γ-rays but is sensitive to cosmic rays in general. Therefore, initially recorded events in the data constituted showers from high energy γ-rays, protons and ionized nuclei. For the purposes of γ-ray astronomy, the hadronic events had to be identified and cast out.

The spatial distance between the γ-ray source, in this case the SNR, and the observatory is vast — probably leading to some delays due to finite signal travel time. The space between such a SNR and the observatory is not necessarily empty, and may host massive or very dense objects which may affect the movement of signals between the two.

These are some of the aspects which introduces 'impurities' in observational data. We now address some of

these issues, by explaining each a little bit more. In addition, we provide in each case, ways and means of doing the required adjustments.

All the same, before manipulating the data in any form, we first have a look at the format and the structure of the data as received. Table 4.1 gives an outline of the γ-ray data from H.E.S.S.

4.2 The Structure of the Data

4.2.1 General Appearance

The supernova remnant MSH 15-52 was observed in 2004 with H.E.S.S. for about 4 months, between 25^{th} of March (53089 MJD)[1] and the 20^{th}July (53206 MJD). The source was detected as an extended DC source, i.e. excess photon arrival events from the direction of the source were recorded. As it should be, these observations were carried out during dark moon periods, bringing the total time of life observation to about 32.3 hours. Hence, the ToAs have intervals of "dead time", where observations were interrupted.

The data (as described herein) refers to the data after all the 'cuts' and 'selection' procedures, which ensures that only γ-ray events from the vicinity of the source are chosen, have been carried out (see § 4.5). We thus refer to data consisting of only γ-ray events.

The entire data set constitutes 119096 γ-ray events with ToAs, selected from a region of about 1° radius around the pulsar. That is, the γ-ray signals taken are from the pulsar as well as the PWN. The event records do not only feature the arrival times, but also gives amongst others, the position (RA & DEC), the energy in (in TeV), and the angular distance from PSR B1509-58. The arrival times are quoted as the time (in seconds) since the 1^{st} of January 1970 00:00 UT. The ToAs have a nanosecond (10^{-9}s) precision.

Periodicity analysis of the data is solely concerned with the time of arrival of the photons. For these reason we extracted only the arrival time entries, and as such, we will make no explicit computations with the other variables in the data set.

[1] MJD stands for Modified Julian Day — a dating convention used in astronomy. It is a variant form of the Julian Date (JD), which is an integer count of days since noon of 1^{st} January 4713 B.C.

Night	Date in 2004	Duration [min]	Number of events	"Run-based" observations
1	25th March	45.6	2884	Obs 1
2	14th April	28.0	1918	Obs 2
3	15th April	89.6	5992	Obs 3
4	16th April	118.8	8776	Obs 4
5	17th April	118.7	8520	Obs 5
6	18th April	118.8	7558	Obs 6
7	19th April	128.9	7915	Obs 7 & 8
8	20th April	118.9	8268	Obs 9
9	21st April	121.3	6222	Obs 10 & 11
10	22nd April	119.1	7978	Obs 12
11	9th June	91.2	6341	Obs 13
12	14th June	28.0	1967	Obs 14
13	15th June	121.2	7586	Obs 15
14	16th June	118.7	4755	Obs 16 & 17
15	17th June	152.8	9489	Obs 18
16	18th June	58.2	3614	Obs 19
17	21st June	60.2	3517	Obs 20
18	13th July	58.3	3515	Obs 21
19	14th July	58.4	3794	Obs 22
20	15th July	28.0	1803	Obs 23
21	16th July	28.1	1644	Obs 24
22	18th July	63.3	2113	Obs 25 & 26
23	20th July	57.7	2927	Obs 27
Total $\Longrightarrow$		**1931.8**	**119096**	

Table 4.1: *The outline of the MSH 15-52 data acquired by H.E.S.S. The SNR was observed over 23 nights, for a total live time of 32.2 hours. The outline also gives the number of γ-ray events recorded each night. The last column shows the run numbers — this is explained in § 4.3.*

4.3 Runs & Observations[2]

During a particular night, H.E.S.S. observes a pre-determined list of sources prescribed by a nominal observation schedule. These schedule may be comprised of surveys of the Galactic plane, AGNs, quasars, SNRs, pulsars, black holes, other galaxies, transient objects, and even gamma-ray bursts (GRBs). The observation schedule is based on the source prioritization and the visibility of objects in the sky at the time in question. This implies that only a fraction of the available observation time in a night, is used for a particular source. This is one way how dead time intervals creeps into the timing data.

[2]The terms *run* and *observation* will be given special meanings here. They will be used to refer to certain segments or portions of data. The splitting of data into runs or observations is done at places where discontinuities or timing gaps of certain lengths are observed, as seen later.

Another, perhaps less prominent, aspect which contributes to dead time gaps in timing data is related to the on-site technical activities. These activities could be delays, failures, or some other kind of inconsistencies at the software, hardware or even environmental level at the site during observations.

Since registering of a pulse arrival is done against real time clock readings, it is inescapable to pay attention to dead time gaps in the data. For this reason we split the bulk data set into nightly observations. A night observation was also subdivided into smaller segments dead time of greater than 10 minutes is observed.

The data consists of 27 'runs' of observations during 23 nights. The term 'run', as used hereafter, is basically the least time interval that H.E.S.S. array is set to track a source — usually around 27 minutes. While a single run last about half an hour, a night observation consist of one or more runs in the same night. Therefore, nightly observations are greater than or equal (in most cases) to run-type data. We subdivide the timing data into 'run-based' and 'night-based' observations as follows:

↪ RUN-BASED DATA SETS

Any given two runs from the same night that are separated by a dead time of > 10 minutes have been split into two 'observations', and is referred to as *run-based.*

↪ NIGHT-BASED DATA SETS

A *night-based* data set is obtained by splitting the data at a dead time of interval > 20 hours between any ToAs.

This division generates the following (see Table 4.1): Four pairs of run-based observations merges to create a night-based data set. These are the 7^{th} and 8^{th} observations making the 7^{th} night data set, the 10^{th} and 11^{th} observations making the 9^{th} night data set, the 16^{th} and 17^{th} observations making the 14^{th} night data set, and lastly the 25^{th} and 26^{th} observations making the 22^{nd} night data set. The rest of the night-based observations consist of single run-based data sets.

The periodicity search was then done on both run-based and night-based data sets. This practice deals with possible smearing out of pulsations by the discontinuities caused by gaps in the data.

4.4 Acquaintance with the Data

Before starting off with rigorous data analysis, it is of great convenience to have a quick 'feel' of the data. Such a rough inspection may, in some cases, give an idea of the nature of the data.

A quick feel may warn or indicate the presence of 'fatal' errors or mistakes in the data, that may otherwise not be easily identified by an involved (or rigorous) analysis technique. As a measure to acquaint ourselves with the data, we performed a speedy check on the number of events recorded per unit time — the mean count rate.

4.4.1 The Count Rate

As a preliminary analysis, we inspected the density of events in a unit time. We were interested in the number of photon arrivals recorded per minute. The ToAs are given in seconds (with a nanosecond accuracy) since 1970 as mentioned earlier. Have a look at the very first ToA, recorded as,

$$\text{ToA}_1 = 1080269808,899669900 \text{ seconds} \tag{4.1}$$

This is a very cumbersome number — it needed some manipulation. Subtracting the same value from all ToAs leaves the difference in spacing between any two successive events unchanged. Hence, we subtracted the value in Equation 4.1 from all the ToAs. This gives convenient values of the arrival times in seconds.

The count rate can now be obtained by binning the data into bins, where the bin width is determined by the time interval of interest. For a small count rate, the bin width was taken as 600s. The number of bins required depends on the range of the data. The range is given by the absolute difference between the first ToA t_1 and the last t_n, as in

$$number\ of\ bins = \left\lceil \frac{t_n - t_1}{bin_{width}} \right\rceil \tag{4.2}$$

where $\lceil x \rceil$ is the *ceil function* giving the smallest integer not less than x.

The histogram obtained from this procedure, where the frequency of entries in a bin is plotted as a function of bin size, is a sufficient display of the count rate. Although a histogram is traditionally represented bars, with thickness defined by the bin width, we can let each bin be represented by a point — making the plot a continuum line as shown in Figure 4.1.

It is seen in Figure 4.1 that about 600 to 800 photon arrivals are detected every 10 minutes. This amounts to a count rate of 60 to 80 events per minute. Thus at minimum, an event is recorded every second. The count rate is at an acceptable level, and does not cause alarm of any peculiarity within the data. Therefore, we accept the data as being of satisfactory standard.

For a much closer look, we singled out a segment of the data to reconfirmed the count rate from a single

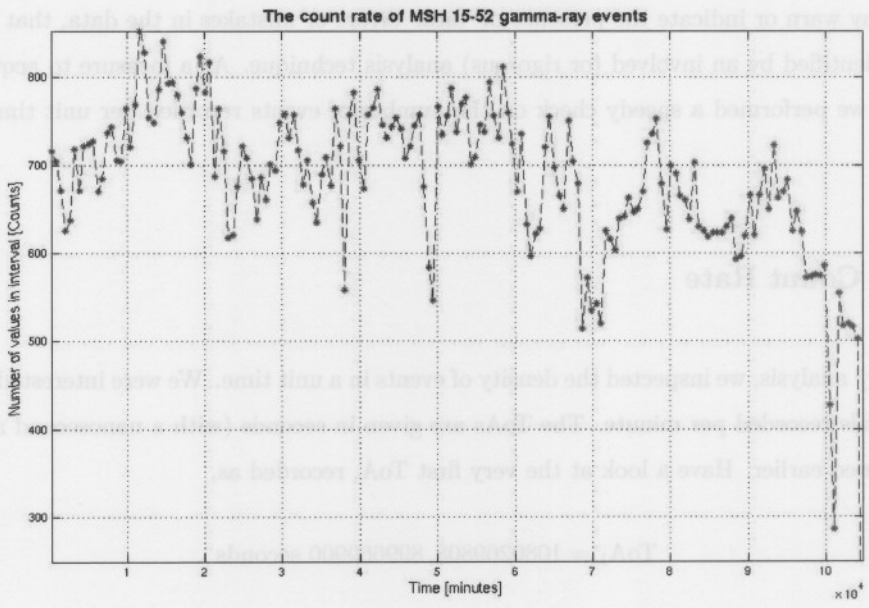

Figure 4.1: *The number of γ-ray events in 10 minute intervals over the complete data set. This plot was obtained by binning the data into bins of 10 minute widths, however each bin is represented by a point to obtain a continuum line, with time on the x-axis.*

night observation. This was done for the observation carried out during the 5^{th} night of observation, and is shown in Figure 4.2. It will be made clear in § 5.2.1 why this particular night data set was selected here.

Figure 4.2 also indicates that the count rate is around the 80/min mark. The count rate is as expected, so much so that one can comfortably go ahead with in-depth data analysis techniques.

4.5 Data Selection

Although the atmosphere is the detection 'agent' in VHE γ-ray astronomy, changes in low-altitude atmospheric conditions also affect the performance of the system, which in turn may affect the quality of the data that is recorded. As stated by Brown et al. (2005) as a worst case scenario: variations in atmospheric quality may lead to a systematic bias in the approximated energy of γ-ray events. It is thus essential that necessary calibrations be done, in order to correct the data for atmospheric instabilities. An calibration for atmospheric correction for H.E.S.S. can be seen in Brown et al. (2005).

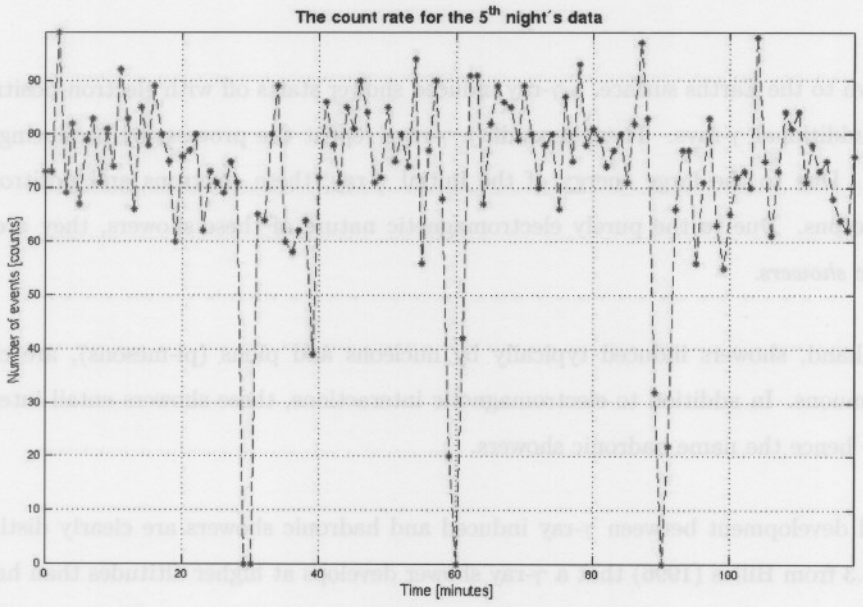

Figure 4.2: *The count rate for a segment (5^{th} night of observation) of the data. Notice that this observation is comprised of 4 runs of about 30 minutes each. The actual duration of this observation is 118.7 minutes.*

As mentioned earlier, the telescope is not only sensitive to γ-rays — it get triggered by cosmic rays in general. Cosmic rays appear mostly in the form of energetic protons or ionized atoms. In fact, this additional hadronic cosmic ray component is very intense and forms a isotropic background (see e.g. Hillas, 1996), such that γ-ray events are in fact rare — because γ-rays come from point-like sources. This fact may may not sound inspiring. Fortunately for us (courtesy of the stereoscopic mode of observation), a γ-ray event selection processes is accurately done by H.E.S.S., prior to dissemination of the data to researchers. The detail of H.E.S.S. data selection criteria, done using 3D reconstruction of γ-ray showers, is explained by Lemoine-Goumard et al. (2006).

The γ-ray selection is done on the principle of differentiating between the showers induced by γ-rays and those induced by protons (hadrons). Due to the difference in the induced showers, the images that are obtained from IACT are also different. The basic idea of selecting γ-rays events is by *rejecting* their counterparts — the hadrons.

4.6 Rejection of Hadrons

On its way down to the Earths surface, a γ-ray induced shower starts off with electron-positron pairs, which in turn emits additional γ-rays. These secondary γ-rays repeat the process, by producing more electron-positron pairs. Due to the large energy of the initial γ-ray, these electrons and positrons leads to the emission of photons. Due to the purely electromagnetic nature of these showers, they are also known as *electromagnetic showers.*

On the other hand, showers induced typically by nucleons and pions (pi-mesons), are characterized by production of muons. In addition to electromagnetic interactions, these showers entail interactions via the strong force — hence the name hadronic showers.

The shape and development between γ-ray induced and hadronic showers are clearly distinguishable. We see in Figure 4.3 from Hillas (1996) that a γ-ray shower develops at higher altitudes than hadronic showers. A hadronic shower also develops into a broadly spread feature while a γ-ray shower is more focused and thus concentrated.

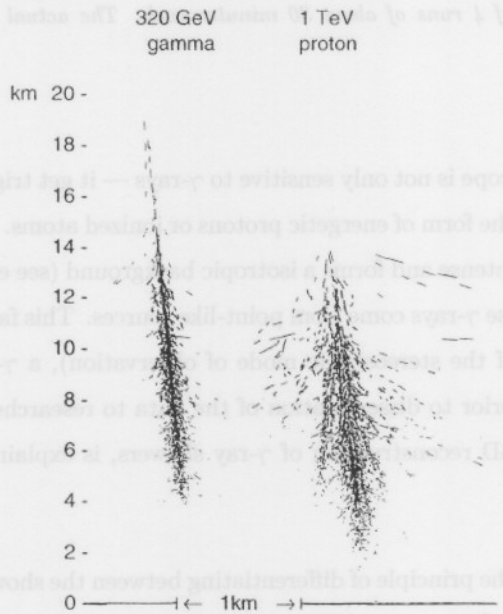

Figure 4.3: *The difference in the lateral and altitudinal development of showers induced by a 0.32 Tev γ-ray (left) and a 1 TeV hadron (right). The γ-ray induced shower is clearly focused, while the hadronic shower exhibits a more pronounced lateral development. This image was taken Hillas (1996).*

The shower images formed in the camera of a CT by γ-rays and hadrons are therefore different. Hadrons

produce irregularly shaped images. On the contrary, narrow elliptical images are formed by γ-ray showers. Image parameters shown in Figure 4.4 (a), called the *Hillas parameters*, describes the shape of the image by means of quantities like width, length, ellipticity and the pointing angle α. Figure 4.4 (b) also shows the difference in the shapes of γ-ray and cosmic ray induced showers.

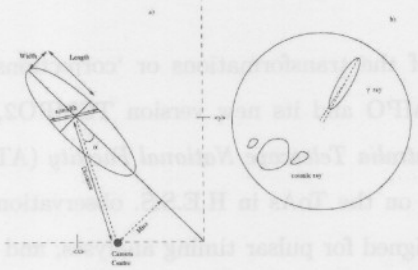

Figure 4.4: *(a) The Hillas parameters, and (b) camera image of a γ-ray versus that of a cosmic ray. Analysis of Hillas parameters (defined by the shape of the image) is useful in determining the origin of a shower. This image was taken from a note by DURHAM-Group (2006).*

The Hillas parameters of a shower image are used to determine the type of particle responsible for the triggering of the telescope. Simply put, imaging cameras are employed to discriminate γ-rays from hadrons.

A more recent development in this regard can be seen in Lemoine-Goumard et al. (2006). The latter describes a method based 3D-modeling of the Cherenkov light emitted by γ-rays which makes it possible to reconstruct γ-ray showers in three-dimensions. The method reduces the parameters required for rejection of hadronic showers by enabling the selection of γ-ray induced showers based only on their *rotational symmetry* and *small lateral spread* (see details in Lemoine-Goumard et al., 2006).

The motivation and realization of the 3D γ-ray shower reconstruction approach is provided by the stereoscopic imaging ability of new ground-based γ-ray systems like H.E.S.S., CANGAROO (Collaboration of Australia and Nippon for a GAmma Ray Observatory in the Outback) and VERITAS (Very Energetic Radiation Imaging Telescope Array System). Stereoscopic imaging has thus improved hadron rejection procedures in γ-ray astronomy.

4.7 Data Correction

The position and motion of Earth with respect to the γ-ray source have considerable effect on the pulse arrival times at the observatory. Cleaning of pulsar timing data thus incorporates the consideration of Earths motion and position, and transforming the ToAs accordingly.

Briefly listed hereafter, are some of the transformations or 'corrections' that needs to be done on the data. Pulsar timing packages, TEMPO and its new version TEMPO2, were developed by astronomers at the *Princeton University* and *Australia Telescope National Facility* (ATNF) do to these transformations. We used TEMPO to do corrections on the ToAs in H.E.S.S. observation data of the supernova remnant, MSH 15-52. These packages are designed for pulsar timing analyses, and as such employs the ephemerides of pulsars as given by the ATNF Pulsar Catalogue described in (Manchester et al., 2004).

4.7.1 Clock Corrections

Pulse arrival times are generally specified in relation to the local observatory clock. As mentioned earlier, the timing data of MSH 15-52 is quoted in UT, which stands for the *Universal Time*[3]. Otherwise also known as the Coordinated Universal Time UTC, this timing system is not convenient when accuracies better than a second is required.

The non-uniform rotation of the Earth around its axis, and in its orbit around the Sun, leads to an irregularity in timing systems. This is conventionally corrected for by incorporating the so-called *leap second*.

The National Institute of Standards and Technology (NIST), based in the U.S., maintains and transmits a time scale that corrects for leap seconds (see NIST, 2006) through various atomic clocks in the world — the UTC(NIST) system. UTC(NIST) is a real time version of the International Atomic Time (TAI).

TEMPO ensures that the pulse arrival times integrates the non-uniform rotation of the Earth by correcting the ToAs with the required leap seconds, based on UTC(NIST) standards.

[3]Also referred to as the *Greenwich Mean Time* GMT, is the time kept on Earth relative to the zeroth longitude near Greenwich, England.

4.7.2 Barycentering ToAs

Pulses from a pulsar may travel shorter distances in some instances than others due to the motion of the Earth in the solar system. It takes the Earth about 12 months to move around the Sun. Pulse signals that travel along the ecliptic plane, arrive earlier at the Earth than at the Sun when the Earth is closest to the source. After 6 months pulses will arrive late at the Earth by approximately the same amount (Lyne & Graham-Smith, 1990). That is to say, the Earth nor the Sun are not convenient inertial reference frames.

The space-time coordinates of pulse arrival events in pulsar timing data are specified in the observatory coordinate frame (Edwards et al., 2006). As pointed out in e.g. Hobbs et al. (2006) pulse arrival times require transformation to an inertial reference frame. The idea is to select an inertial reference just within the solar system.

A suitable local inertial reference frame is the center of gravity of the solar system, better known as the *Solar System Barycentre* (SSB). Due to the large mass of the Sun, with respect to other solar bodies, the SSB lies closer to the Sun than other bodies in the solar system. As Lyne & Graham-Smith (1990) puts it, the motion of the Sun in relation to the SSB is a result of the orbital motion of other planets — especially Jupiter, whose mass places the barycentre *just outside* the surface of the Sun. The Solar System Barycentre is a quasi-inertial frame (Edwards et al., 2006). The transformation of the photon arrival times to the SSB's frame is called the *barycentric correction* or simply *barycentering* — a process that requires the exact position coordinates of the observatory on Earth.

The following are aspects that are considered in the barycentric correction process.

↪ The Einstein Delay

The observatory frame and the frame of the SSB are related by a relativistic 4D space-time transformation (Edwards et al., 2006). The relativistic time dilation and the gravitational redshift (Einstein delay) that the signals experiences, are corrected for with this transformation.

↪ The Roemer Delay

The pulse signal from the pulsar has a longer distance to travel, when the Earth is at the far end (from pulsar) of its ecliptic orbit. The signal arrival time is then retarded. The correction involves the transformation of the observatory position from the terrestrial frame to the celestial reference frame (Edwards et al., 2006).

↪ The Shapiro Delay

The Shapiro delay is a direct implication of the Einstein's theory of general relativity. Predicted by Irwin Shapiro, this was one of the first measurements that put general relativity to test (Hartle, 2003).

The Shapiro time delay refers to the delay in the propagation of light, when passing near an object with large gravitational field such as the Sun. The path of the light signal is curved as it gets deflected by the Sun (see e.g. Hartle, 2003).

↪ DISPERSION MEASURE

Gamma-ray arrival tmes is not notably affected by "dispersion measure". Nevertheless, it is a common concept in the sister astronomy — radio astronomy.

Radio signals suffer a frequency dispersion in arrival time due the ionized ISM. This delay in the arrival time depends on the electron content and the distance between the observatory and the pulsar. These parameters, together with the observing radio frequency of the telescope are used to define a variable known as the *dispersion measure* DM in pc/cm^3, which in turn gives the time delay in seconds as (Lyne & Graham-Smith, 1990)

$$\Delta t = 4.15 \times 10^3 \, DM \, \nu_{obs}^{-2} \tag{4.3}$$

where ν_{obs} is the observing frequency in MHz. For the present case, the DM of pulsar B1509-58 is 252.5 pc/cm^3 while a typical γ-ray energy is of the order of $E = 1$TeV. If one assumes the relation $E = h\,\nu_{obs}$, then the observing frequency is of the order 10^{20} MHz, resulting in a very negligible amount of delay time of $\sim 10^{-35}$ seconds. Hence, we do not need corrections for the dispersion measure. Dispersion measures of various radio pulsars can be seen in e.g. the ATNF pulsar catalogue. Given the pulsar ephemerides, TEMPO corrects the ToAs for frequency dispersion.

These effects may be small compared to our precision. Nevertheless, analyzing timing data of a millisecond pulsar requires the best possible accuracy, and as such we have to do the applicable corrections. The TEMPO software was used to effect timing corrections of the data. The technical procedure for using TEMPO is given in more detail in Appendix A.

Chapter 5

Periodicity Search Results

> "A test is consistent against a given light curve shape if the significance of the detection improves as more data are added under fixed conditions" — de Jager et al. (1989)

5.1 Introduction

THE periodicity of γ-ray emission from the supernova remnant MSH 15-52 was search for, by means of the tests for uniformity on the circle, as described in Chapter 3. The arrival times were folded on the phase interval $[0, 2\pi]$, using the values of the pulsar frequency and its derivatives as given in Table 2.1. This was done for a number of period values around the expected radio period of the pulsar — giving a range for searching in period. This period domain defined as 3 IFS on either side of the expected radio period.

The phases were then used to obtain various statistics of the tests for uniformity of the phases on the circle. The test statistic in turn gives the observed p-value (p-level) or the observed significance, which is then compared against the detection threshold. The latter, the detection threshold, is set at the 10^{-4} level, although this value depends on the actual number degrees of freedom as mentioned in Chapter 3.

For observed p-values that are $< 10^{-4}$, we reject the null hypothesis — rejecting the hypothesis that the phases are uniformly distributed on the circle. Or in other words, we accept the hypothesis that the emission is pulsed at the corresponding period. Such a result in effect marks the discovery of a periodicity in the photon arrival times.

Alternative to checking for the observed p-value, one can also consider analyzing the observed significance

as a function of the test period — the type of periodograms which will be dominantly studied here. The relationship between the p-value and the significance, given in Equation 3.14 can allow us to obtain the detection threshold (of 10^{-4} or even lower depending on the degrees of freedom) in terms of the significance:

$$\begin{aligned} significance &\equiv -\log_{10}(p\text{-}level) \\ &= 4 \end{aligned} \tag{5.1}$$

That means, we can claim the discovery of a pulsed signal (for a given test period) if the observed significance for that period is larger than 4.

The various test and techniques introduced in Chapter 3, are suitable in certain optimum conditions. On the contrary, there are thus conditions under which a certain testing technique may not be ideal. For example, the Rayleigh test is conventionally good for pulse signals that depicts sinusoidal light curves.

The length of the data set (or its size) also plays an important role in the success of a test. Extremely long duration observations contains large number of events. The signal strength of a detectable signal in an observation with n events, is given by

$$signal\ strength \approx \frac{\sqrt{n}}{n} \tag{5.2}$$

Hence, for long observations with large n, the signal strength of a detectable signal decreases. Therefore, with long observations, pulses with a weak signal strength can be detected — the sensitivity to faint pulses increases.

Unfortunately, large duration data sets may suffer significantly from situations where the pulse phases are not *coherent*[1]. Incoherency in a pulse phase can be dealt with best by the shortest possible scan or observation, which in turn reduces the sensitivity to detect weak signals.

Considering the above-mentioned effects, we developed a scheme for the periodicity search. Table 5.1 gives an outline of the scenarios we investigated for the periodicity search. There it can be noticed that the Eadie combination technique, as used herein, uses night-based data sets that are relatively short. Therefore, this technique tends to be good for data where the phase is not locked. However, this combinatory method may imply that a pulsed signal in a few nights may be diminished by those night data with no pulsed signals. Also note that the run-based data sets are regarded as the smallest quanta, corresponding to the best sets for non-coherent data — with weak sensitivity to faint pulsed signals.

[1] Coherency of a pulse is characterized by the pulse consistency on the phase interval, such that the pulse is located at the same position on the phase interval in each cycle. A coherent light curve is said to be *locked in phase* — while incoherent light curve exhibits a phase modulation.

Procedure	Suitable for (pros)	Drawbacks (cons)
Rayleigh test	sinusoidal light curve	not suitable for non-sinusoidal light curve
H-test	non-sinusoidal light curves	no obvious disadvantage
Run-based data test	non-coherent phase data can detect flares	sensitivity to faint pulses decreases
Aggregate data test	sensitive to faint pulses	not suitable when phase is non-coherent
Eadie combination	non-coherent phase data	signal may be reduced

Table 5.1: *The outline of various periodicity test scenarios. Note that each testing procedure features advantages and disadvantages, and since the true mode of emission is not known it is advisable to explore all of these approaches.*

We reason that the testing procedures shown in Table 5.1 is an exhaustive approach when nothing is known of the form of the periodic emission and its light curve. This broad approach is also recommendable as there is uncertainty in the possible periodicity.

5.2 Rayleigh Results

As outlined in Chapter 4, the acquired data consists of 27 runs[2] of observations during 23 nights over a period of almost 4 months, between March and July 2004 — giving live observation time of 32.3 hours. In what follows, we give the Rayleigh test results for run- , and night-based observations. The Rayleigh test is considered to be most suitable in the event where the light curve is sinusoidal (see Table 5.1).

As the aim of this work is to determine the periodicity of the events in these data sets, only those results that return the greatest evidence or those with special features will be shown — omitting statistical insignificant or uninspiring results.

5.2.1 Run-based Results

We first look at the results for short runs, where the test is sensitive to coherently pulsed data. The best significance achieved comes from the 5^{th} run-based observation performed in April 2004. The plot in Figure 5.1 shows this result.

In Figure 5.1, the expected radio period is located exactly in the middle of the period domain, as indicated with a double arrow. The period range, obtained by taking 3 IFS on either side of the test period, runs

[2]For the definition of the term 'run', as used here, refer to § 4.3

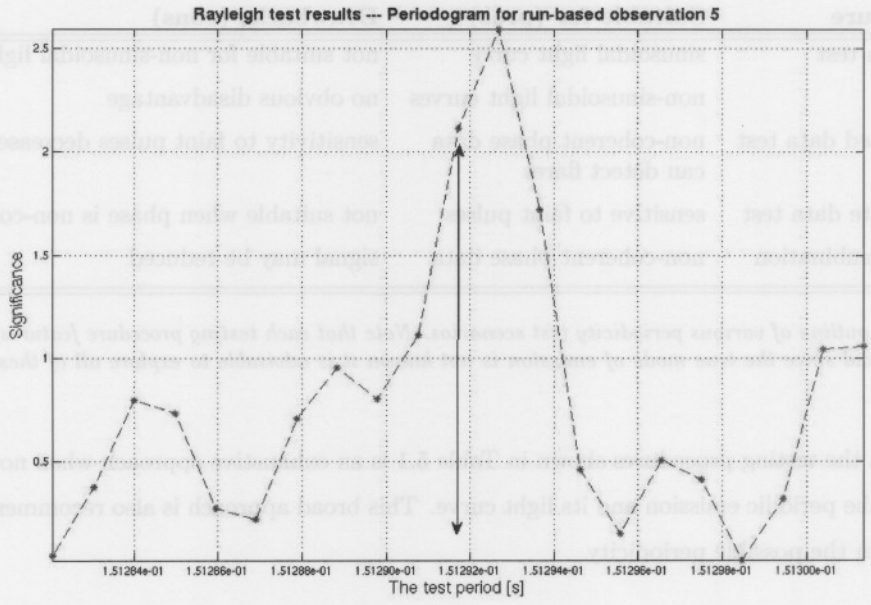

Figure 5.1: *The run-based Rayleigh test result with the greatest significance. The data point of the expected radio period is shown with a double arrow, while the period domain centered at the expected period was obtained by taking 3 IFS steps on either side of the it. The peak lies within 1 IFS from the expected value, at* 151.293 *ms, where* IFS $= 1.4 \times 10^{-4}$ *s. Note: The error bars are smaller than the data points on all the graphs shown herein (see Appendix B).*

along the horizontal axis, with an IFS of 1.4×10^{-4} s.

The significance at the expected period is located slightly to the left of the peak in Figure 5.1 with a value of about 2.2. The peak value is at a 2.6 significance level within one IFS from the expected value — the highest significance obtained. Although this is the greatest significance, it is only about 65% of the detection threshold as required in Equation 5.1. Even though it indicates no significant level of periodicity, this result is inspiring. Once more, this result features the best, almost centrally located peak near the expected periodicity. Though this result seems to indicate the presence of a pulsed signal near $P = 151.293$ ms — claiming a discovery of periodicity does *not* have a sound statistical weight, given that the detection significance of 4 is not met.

5.2.2 Night-based Results

One would like to investigate the Rayleigh test results when considering per-night observations — arrival time events separated by not less than 20 hours. Since most scans of MSH 15-52 in a night were almost continuous, with dead time of only a few minutes, the run-based data sets are mostly the same as the night-based data sets. The simple and obvious example would be a night where only two runs of about half an hour each (separated by a minute) were performed — the run-data set would be the same as the entire night data set.

It can be seen from Table 4.1 that only four night-based data sets differ from run-based data throughout the entire MSH 15-52 scan of almost four months. The implication here is that the best night-based result can only be chosen from 4 nights. These are night 7, night 9, night 14, and night 22. Each of the night numbers not listed are equivalent to some run-based observation (consult Table 4.1).

The greatest significance obtained on a night-based approach, is from the data of the 7^{th} night. The other three night data sets yielded significance much lower than night 7. The results of this data set is shown in Figure 5.2.

The curve seen in Figure 5.2 clearly shows the relatively large jump in the significance up the about 2.3, compared to the base line of the data. The peak lies at about three IFS (where IFS $= 1.3 \times 10^{-4}$ s) from the radio period, at 151.285 ms. The latter, shown with an arrow in Figure 5.2 has a negligible significance. However, the maximum significance of 2.3 is not large enough for a detection of a pulsed signal at that period.

Given that the run-based data and the night-based data are mostly identical, it suffices to only consider the night observations in the work that follows. That is, any result that is shown from here on, is from one of the 23 night data sets, unless otherwise stated.

5.3 The H-test Results

The H-test, initially proposed by de Jager et al. (1989), was introduced in § 3.9 as an improvement on the Rayleigh test. This makes the Rayleigh test the special case of the H-test. In essence, the Rayleigh test only measures the power of the first harmonic, while the H-test checks the power for the first 20 harmonics. By employing the H-test we therefore carry out a broader investigation of the power in the harmonics, than in the Rayleigh test. As stated in Table 5.1, the H-test approach is suitable for non-sinusoidal light curves.

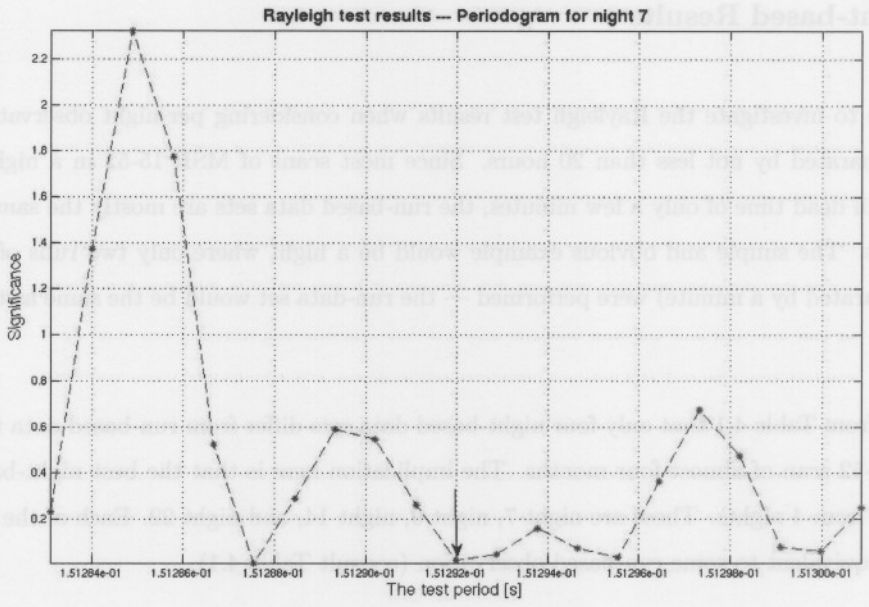

Figure 5.2: *The night-based Rayleigh test result with the greatest significance of about* 2.3. *The data point of the expected radio period is shown with an arrow, having a negligible significance. The peak lies at about 3 IFS towards the left of the expected value, at* 151.285 *ms. One IFS is equal to* 1.3×10^{-4} *s. The complete period range amounts to 6 IFS centered at the radio period.*

The process of executing the H-test is similar to that of the Rayleigh test. The difference lies in the computation involving the phases — the phases in the Rayleigh test goes like ϕ_i, while the phases in the H-test are defined by $\ell\,\phi_i$ for $\ell = 1, 2, 3, \cdots, 20$. The level of significance of the first harmonic is tested when ℓ is strictly one, while letting ℓ take on various positive integers produces the significance of various harmonics. The H-test computes the largest significance from the first 20 harmonics obtained in doing so. As explained in Chapter 3, the process involves calculation of the Z_m^2 statistic, with $2m$ degrees of freedom. In these case, m is the harmonic number. For large n, the Z_m^2 statistic tends to be χ^2-distributed. One then gets the H-test statistic $\mathcal{H}$, by selecting the maximized value $Z_M^2 - 4M + 4$, as defined in Equation 3.16. Values of $\mathcal{H}$ are then used, along with χ^2-tables (see § 3.9), to get the respective significance.

The result with the greatest significance obtained from the H-test is exactly identical to the best result from the Rayleigh test shown in Figure 5.1. From these data, from night 5, it was seen that the maximum significance of 2.6 is achieved within 1 IFS from the expected period.

Generally, the results obtained from the H-test largely corresponds with those from the Rayleigh test — in fact for most of the data sets, the two results are indistinguishable. Although there are eleven data sets that

shows differences in the results from the two techniques, the differences are very small — generally either increasing or decreasing the significance with about 0.1 at one data point only. The largest such deviation between the Rayleigh test result and the H-test result, is shown in Figure 5.3.

In the data from night 16 in Figure 5.3, the data points shown with rectangular blocks shows the difference in the significance as obtained by the two test. Figure 5.3(a) represents the Rayleigh test results, while the H-test results can be seen in Figure 5.3(b).

Figure 5.3 has the largest observed difference between results from the two tests. The significance at about 3 IFS to the left of the expected period was obtained as 0.2 with the Rayleigh test, and just above 1 with the H-test. The difference is about 0.9. In any case, this new H-test value is also not of the desired significance level as far as the periodicity search is concerned.

The other deviations seen in Figure 5.3 located at about 2 IFS to the left from the radio period, and about 3 IFS to the right of it, are small.

The difference in these values are attributed to the fact that the H-test selects the harmonic with the largest power. Hence, the significance of that particular test period deviates from the value initially obtained from the Rayleigh test. Given that the two test predominantly yields the same results, it can be concluded that the fundamental harmonic generally seems to be the most powerful harmonic.

5.3.1 Eadie Results

Results from individual observations failed to statistically challenge the null hypothesis. However, as discussed in § 3.10, we can combine the p-values $\{p_i\}$, resulting from the Rayleigh test, from these individual observations to determine the significance of all the data sets combined. This approach is best for non-coherent pulsed data, as described in Table 5.1. Equation 3.17, shows how *Eadie combination*[3] of p-values is done.

As explained in Chapter 3, the procedure involves assembling of p-values obtained from the Rayleigh test for *a given test period* for different observations, and computing a *compound* value Z (χ^2 value) through Equation 3.17. The latter has a χ^2 distribution with $2k$ degrees of freedom, and as such one can read off the corresponding probability from a χ^2 table. This probability (or p-level) in turn gives the 'new' *compound* significance via Equation 3.14. In this case, the combination was done for 23 nights, thus k = 23, such that

[3] *Eadie combination* is a term designated herein, to refer to the p-value combination described in § 3.10. The name *Eadie* is used in the terminology because of the appearance of this technique in Eadie et al. (1971).

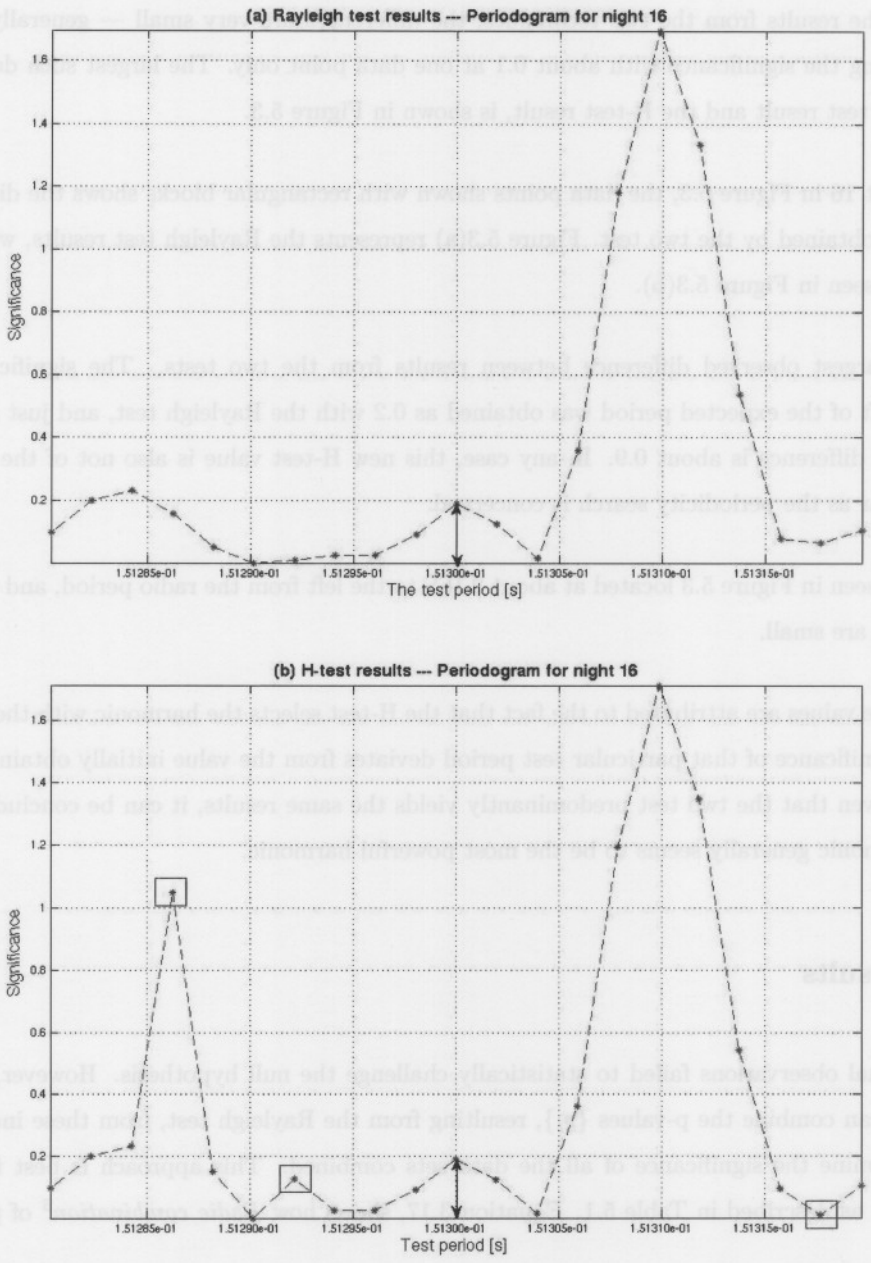

Figure 5.3: *Periodograms with the largest difference recorded between the (a) the Rayleigh test and (b) the H-test results. These two results have a similar overall profile except for the differences shown in part (b) with open blocks. For three test periods, with blocks, the H-test discovered that the most powerful harmonic was not the fundamental harmonic. A total of 6 IFS made the period range along the horizontal axis, with the extrapolated radio period at the center (shown with a double arrow). One IFS amounts to* 2.9×10^{-4} *s.*

we get 46 degrees of freedom.

The Eadie combination technique produces one graph, where the compound significance is given as a function of the test period. Once more, the test period is obtained by considering 3 IFS steps on either side of the extrapolated radio period. The Eadie combination result is shown in Figure 5.4. As the individual data sets has different lengths, an average IFS of 1.8×10^{-4} s was assumed.

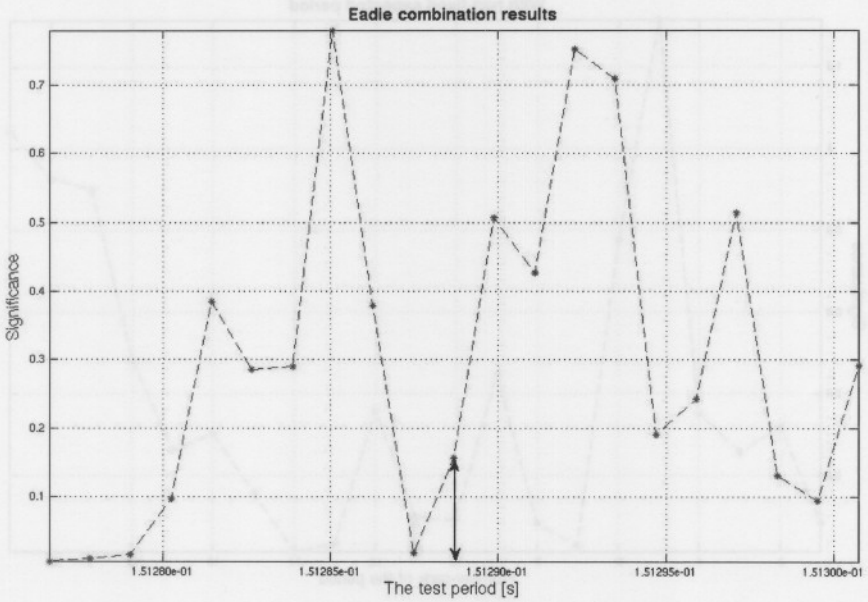

Figure 5.4: *Eadie combination result for 23 night observations. Notice the significance that is less than one across the period domain considered. The expected radio period is the same for all nights. The period range covers a total of 6 IFS centered at the extrapolated radio period of the pulsar.*

The graph shown in Figure 5.4 does not indicate the presence of any significant periodicity. The significance is generally below the 0.8 level. Therefore, we conclude that the Eadie combination approach has discovered no indication of a statistically significant pulsed signal.

With the Eadie combination method not having improved the results obtained this far — a slight adjustment was considered concerning the use of the extrapolated radio period. In the conventional case (Figure 5.4), the expected radio period was computed with reference to the very beginning of the entire observation schedule. This implies that a unique value served as the expected period for all nights.

The slight adjustment was to consider an expected period for each night — depending on the first event arrival time of that night. With this approach each night observation is tested for different period values.

Although this approach might sound realistic, the Eadie combination has to be done for period values that are slightly different but are at the same position away from the expected test period. That means the periodogram will not have absolute period values in seconds along the horizontal axis, but that these will can only be represented by position numbers (ranks) as shown in Figure 5.5. Numbering the lowest period value (at the extreme left) as number 1, the expected period will be the 11^{th}. The number of IFS steps from the expected period is still 3 from it, with average IFS $= 1.8 \times 10^{-4}$ s.

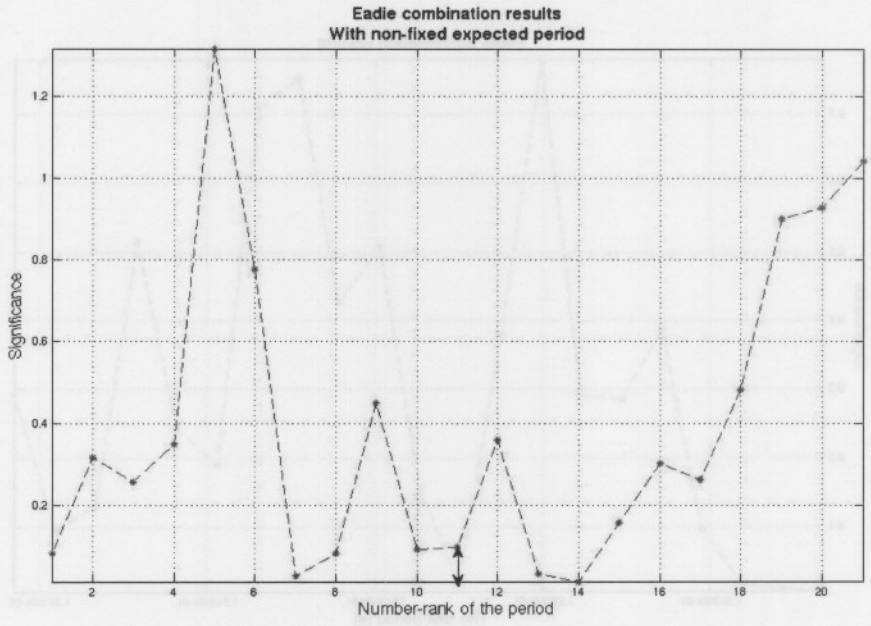

Figure 5.5: *Eadie combination result for 23 night observations. Note that the horizontal axis only gives the position of the test period and not a numerical value, because each night data is tested for a different period range. The period range covers a total of 6 IFS centered at the extrapolated radio period (number 11) of the pulsar.*

The adjustment in the calculation of the expected period, resulting in Figure 5.5, does not improve the significance as desired if periodicity is assumed. The maximum significance observed in Figure 5.5 is just about 1.3 — which is not of great significance, but larger than the significance in Figure 5.4.

The period adjustment performed in order to obtain Figure 5.5 is small, e.g. the largest expected period difference is between that of night 1 (which also happens to be the expected period in Figure 5.4) and night 23, computed as $\Delta P = 151.304 - 151.289 = 0.015$ ms. However, it is noteworthy how this slight adjustment in the expected period produces vastly different results shown in Figures 5.4 and 5.5.

Seen from these results the Eadie combination method did not improve on the results of individually con-

sidered observations. Therefore, the null hypothesis which suggest that the ToAs are uniformly distributed, has not been challenged by the Eadie combination method.

5.3.2 Aggregate Data Results

The significance testing was thus far done for individual observations of the data. In addition, it was investigated if the significance obtained from individual night observation data sets combine into an enhanced significance. Now we look at the bulk of the data as an unitary set. As given in Table 5.1, this approach should render an improved sensitivity to weak coherent signals since the sample size n is the largest. This entire set of ToAs, which spans almost four months, will hereafter be called the *aggregate data set.*

Considering the aggregate data set, the Rayleigh test was carried out for a time series that consist of $n = 119096$ time stamps. That is, the number of ToAs n, increases from about a few thousand (for night-based data) to the order of 10^5. In addition, the 3.9 month duration implies a very small IFS of about 9.9×10^{-8} s, obtained from the approximation in Equation 3.5. As seen in Table 5.1, any incoherency in the pulse phase of such a signal will negatively affect analysis.

The Raleigh test results for the aggregate data set is shown in Figure 5.6. Apart from the multi-peak structure that it features, Figure 5.6 exhibits one of the lowest significance distribution obtained.

The significance obtained in Figure 5.6 is not suggestive of any significant deviation from uniformity. The maximum significance is less than 0.9. Therefore, the minimum p-level is $10^{-0.9} \approx 10^{-2}$, which is two orders of magnitude larger then the required 10^{-4} level. However, the cyclic-type of behaviour seen in Figure 5.6 seems to be increasing in amplitude towards the left.

In order to view the increasing tendency of the significance in Figure 5.6, the number of IFS were increased from 3 to 10 on either side of the expected period. The new result with a larger period range can be seen in Figure 5.7.

The increasing tendency in the height of the peaks in Figure 5.6 seems not to be considerable when viewed over the broader period domain in Figure 5.7. It is clear that subjecting the aggregate data set to the Rayleigh test for a range of periods yielded no significant periodicity.

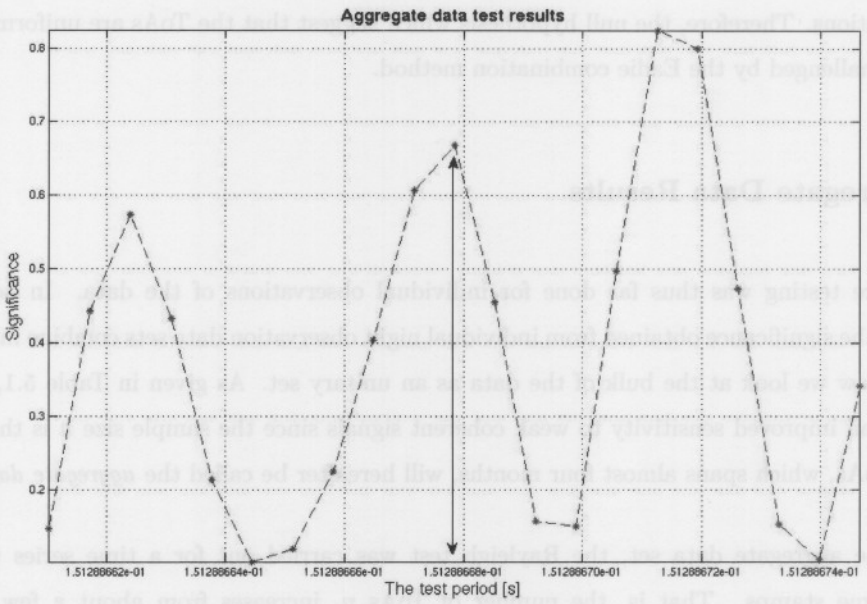

Figure 5.6: *Result from the test on the aggregate data. This represents the Rayleigh test results with an IFS of* $9,9 \times 10^{-8}$ *s, and with the number of photon arrival times* $n = 119096$. *This represents a very sensitive approach in searching for a weak coherent pulsed signal.*

5.3.3 Special Result

In these section we would like to study a result which has a different profile than the other results. Most results have been seen to feature either 'flat-like' or 'irregular' profiles. One would like to draw the reader's attention to the result shown in Figure 5.8(a), which seems to exhibit a persisting increase in the significance, in the direction of decreasing test period. This result is obtained from the data captured during night 14 of the observation programme.

Following the curve from the extreme right to the left (in Figure 5.8(a)) one can see a very clear progressive increase in significance reaching up a significance of about 2.3. This is an encouraging result, in the sense that one would reckon that the increasing tendency in the significance may reach the detection threshold. Suggesting that the arrival times are pulsed at some period lower than the expected radio period. Unfortunately, the narrow period range does not allow a complete evaluation of the increasing tendency of the significance.

To open up this period range, we increase the number of IFS from 3 up to 10 IFS on either side of the test

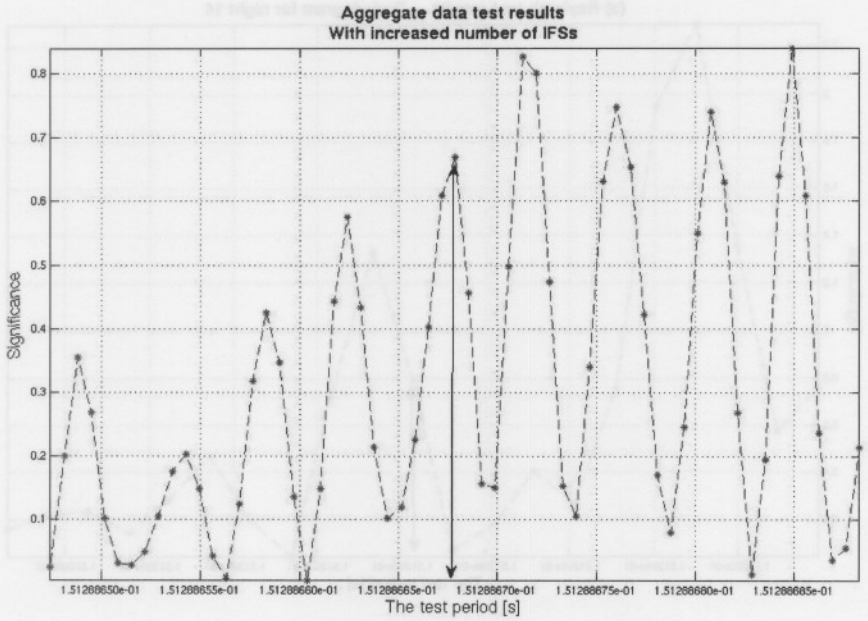

Figure 5.7: *Result from the test on the aggregate data, where the period range have been widened in order to investigate the increasing tendency of the amplitudes of the peaks in Figure 5.6. As seen here, this tendency seems to continue but is still below the detection level. The period range was created by taking 10 IFS steps on either side of the expected period (shown with a double arrow).*

period. This gives a total of 61 test periods. The new result with this adjustment is given in Figure 5.8(b). We notice that the seeming persistent tendency of the significance to increase beyond the period range of Figure 5.8(a), does not prevail.

We have thus exhausted the testing scenarios that were formulated in Table 5.1. The Rayleigh test was performed on short run data, intermediately long night data, and the very long aggregate data. The H-test was performed with virtually the same results. This profound approach ensured that we test the data for cases where the underlying light curve is either sinusoidal or non-sinusoidal — as well as cases where the pulsed mission (if any) is coherent or non-coherent in phase. However, all combinations in Table 5.1 led to statistically insignificant results.

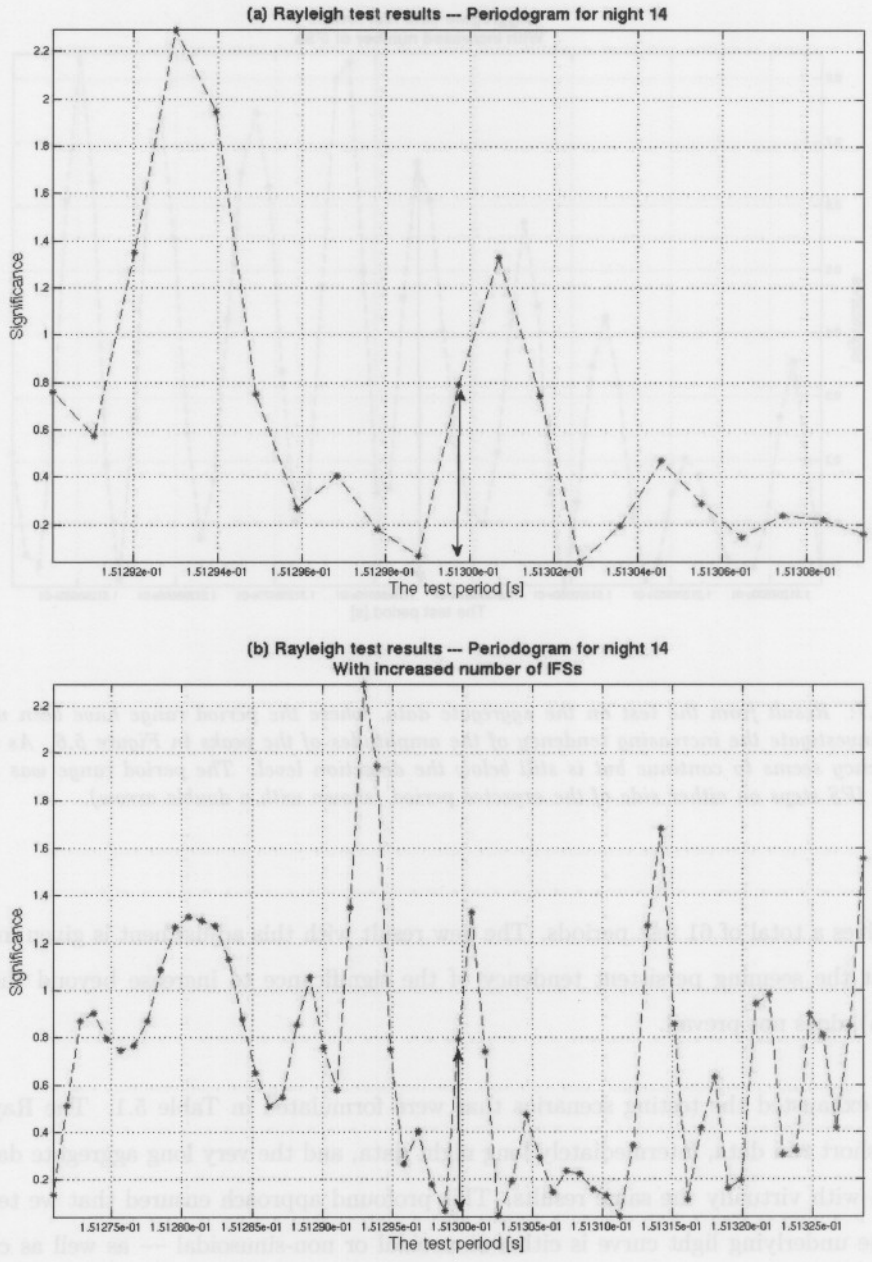

Figure 5.8: *(a) A special inspiring result from the fourteenth night of observation. The special feature is the seemingly progressive increase in the significance towards the left. (b) An expanded view of the special result shown in part (a) — having increased the number of IFS to 10 we notice that this result is still statistically insignificant. Three IFS were taken in either direction from the expected period, where* IFS $= 1.4 \times 10^{-4}$ *s.*

Chapter 6

Summary & Conclusion

> "The data have been subjected to a Rayleigh test for periodicity at a small range of periods around the BATSE period. Phase coherence between observations was not assumed. No significant periodicity was detected, ···"
> — Chadwick et al. (2000)

QUITE recently, numerous discoveries of SNRs by the H.E.S.S. galactic survey were reported. H.E.S.S. discovered 10 'new' VHE γ-ray sources that are conceived as SNRs (Gallant, 2006), of which 6 are considered to be associated with pulsars. In addition, four well-known SNRs, the Crab Nebula, Vela SNR, MSH 15-52 and SNR G0.9+0.1 were observed, revealing VHE γ-ray emission from these sources. This project was motivated by these exciting advances in VHE γ-ray astronomy.

It has also been revealed that no pulsed γ-ray emission *at the radio period* was observed from the Crab, Vela and B1706-44 pulsars (Konopelko et al., 2005). Even more, a periodicity search of γ-ray emission from 11 young pulsars done with H.E.S.S. data, showed no pulsed emission from any of these pulsars at the radio period (Aharonian et al., 2006d). The list of these pulsars included PSR B1509-58 and the three pulsars mentioned in the report by Konopelko et al. (2005). The absence of a pulsed γ-ray signal in well-known pulsars, like PSR B1509-58, needs a deeper scrutiny.

The growing population of VHE sources, and the discovery of unpulsed γ-ray emission from known sources were the driving factors of this project. There was a need to establish the extent of the periodicity of VHE γ-ray emission from a PWN in which a pulsar typically resides. We search for pulsed VHE γ-ray emission from the supernova remnant MSH 15-52. As opposed to a "blind search", where no frequency whatsoever is known, this search was based on the known radio period of the pulsar B1509-58 which resides in SNR MSH 15-52. As such this search is relatively simple compared to the computational demand of a blind search. The nebula

region considered constitutes a region of 1° radius around the pulsar.

The arrival times of γ-ray photons from the source, recorded by the H.E.S.S. telescope array during 2004, constitute the data set on which the search was done. The basic hypothesis was to assume no pulsed signal — the performed test had to prove otherwise. The concept of statistical significance testing was employed for this task. The photon arrival times, considered as circular data, were tested for uniformity on the circle through some likelihood tests. The Rayleigh test and the broader H-test, were used as tests for uniformity. The Rayleigh test investigates the power in the fundamental harmonic, while the H-test does it for the first 20 harmonics. An additional method, called the Eadie approach, was also considered for detecting an incoherent pulsed signal, from a collection of various sets of data,

The Rayleigh test applied to individual runs, searching between 151.282 and 151.301 ms, yielded the maximum significance from the data obtained from the 5^{th} run, which recorded 8520 γ-ray events in 119 minutes. The significance obtained was 2.6 at a period of 151.293 ms located within 1 IFS from the extrapolated radio period, where IFS $= 1.4 \times 10^{-4}$ s. This result does not indicate detection of a pulsed signal. The logical conclusion is that, the light curve represented by the analyzed data is not sinusoidal, if at all periodic. This rules out the possibility that there exist a coherent pulsed signal in the data from MSH15-52, lasting 119 minutes, with a signal strength $> \frac{1}{\sqrt{n}} \sim 1\%$ (see Equation 5.2).

On the next level, the data were considered on a nightly basis. There were four sets of night data that were different from run data. The Rayleigh test established the largest significance from the data of the seventh night as 2.3. This peak value was observed about 3 IFS from the expected radio period at 151.285 ms, where IFS $= 1.3 \times 10^{-4}$ s. Once more, this is a non-detection.

The other possible way that one can detect non-coherent pulsed signals, is by the so-called Eadie combination approach. This technique is based on the idea that insignificant results from various observations can be combined to investigate if the combined significance may be enhanced. The p-levels observed for a test period for each of the 23 nights were obtained from the Rayleigh test, then these p-levels were Eadie combined to get the compound significance. The result of this operation was that the maximum significance was 0.8, at one IFS away from the expected radio period at 151.285 ms. Since each night's data has a different observation duration, an average IFS of 1.8×10^{-4} s was used. The result does not reach the detection threshold, the Eadie combination method suggest that there were no strong flares or non-coherent pulsed emission, with a duration of 120 minutes.

One may assume that there is a weak pulsed signal in the data. Fortunately in that case, the approach of analyzing the aggregate data set, with $n = 119096$, ensures that the test becomes sensitive to very weak signals. The aggregate data set was subjected to the Rayleigh test, searching between 151.288661 and

151.288675 ms, yielding a maximum significance of 0.83 at 151.288671 ms. This peak was observed about 2 IFS from the extrapolated radio period, where IFS $= 9.9 \times 10^{-8}$ s. The time duration here was 3.9 months. This result represents a highly insignificant periodicity — yet the test is sensitive to weak signals. One can only deduce that there is no weak, coherent pulsed signal in these data, with a signal strength of $> \frac{1}{\sqrt{n}} \sim 0.3\%$.

Considering non-sinusoidal pulsed emission, the H-test was applied to single night data. The maximum significance observed with the H-test is the same as that observed by the Rayleigh test, mentioned earlier. That is, the best significance achieved, which does not reach the detection threshold, with the H-test is at the 2.6 level, at 151.293 ms from data of night 5. But the H-test is sensitive to non-sinusoidal light curves, in general. An implication of this result is that the true light curve of the data does not have periodicity. It should be noted that the results from the H-test and those from the Rayleigh test were predominantly similar.

> All in all, no pulsed emission of VHE γ-rays from the supernova remnant MSH15-52 was found in the exhaustive search for periodicity that was carried out. The pulse arrival times are concluded to be random — so that the emission of VHE γ-rays from a region of about 1° radius around the pulsar B1509-58, is non-periodic at *and* near the pulsar radio period.

In a periodicity search *at* the radio periods of 13 pulsars (including pulsar B1509-58), it can be noted that Schlenker (2005) imposed energy cuts on the VHE γ-ray events — and considered the data in two energy bands. The result was that there was some indication that high energy data tend towards periodicity, but the periodicity was not statistically significant.

It is conventionally accepted that emission from rotation powered pulsars, like PSR B1509-58, has a magnetospheric origin — resulting from the interactions of particles with the pulsar magnetosphere. If so, it could be that the unpulsed emission from the surrounding diffuse nebula smears out the pulsation in the observed data. Otherwise, this highlights the non-magnetospheric origin of the observed VHE-γ-ray emission.

The prospects of lower energy observations, with improved detection sensitivity, hopefully with the coming ground-based H.E.S.S. Phase II and the space-based GLAST (the Gamma Ray Large Area Space Telescope) may resolve the issues regarding the absence of pulsed VHE γ-rays in sources that are otherwise known to be pulsed in radio and X-ray energies.

Acknowledgments

Completing this dissertation has been a wonderful and often overwhelming experience. I learned a great deal over a broad spectrum of aspects, including amongst others physics knowledge, programming, and research skills. I have been very privileged to work with one of the pioneers of gamma-ray astronomy in South Africa, Prof Christo Raubenheimer — whose ever-present hard work, endurance and patience created a platform for my birth and growth in gamma-ray astronomy.

I am equally indebted to thank the members and management of the Department of Physics and the Unit for Space Research at the North-West University (NWU) in South Africa for the all the logistics, facilities and stimulating environment that directly lead to the successful completion of this work. Special thanks goes to Ms Petro Sieberhagen and Ms Lizelle le Roux for their kind daily assistance on the administrative end — while Mr Mathew Holleran's expertise in information technology was vital in settling PC end-user issues. I also highly value the uncountably many informative discussions with my close friends, Sibusiso Nkosi, Golden Nyambuya and Donald Ngobeni, in no preferred order.

It will not be possible to list all individuals that contributed in one way or other, either in greater or lesser amount, to the actualization of this dissertation or to my well-being during the course of this project — even though they are not listed, their contributions are highly appreciated.

It is indeed a pleasure to thank Dr Riaan Steenkamp from the University of Namibia (UNAM), for having stimulated my interest for postgraduate studies and Space Physics in particular — I thank Riaan for introducing me to the North-West University. I am grateful to the head of the Physics Department, Prof James Oyedele, and colleagues at UNAM, for having strongly and effectively supported the leave that I needed for full-time studies, while they had to be overloaded with the workload I left behind.

This studies would not have been realized without the timely financial support from the Africa-America Institute (AAI). Special thanks goes to Ms Liouse Africa, the AAI representative in Johannesburg, for her prompt and motherly approach in handling financial matters throughout my studies.

Lastly, yet not the least, I wish to thank my parents, Eliza Dai and late Festus Hainuca. For they bore, raised, and loved me. I dedicate this dissertation to them.

Appendix A

The TEMPO Package

A.1 Introduction

TEMPO is a software package designed for pulsar timing data. This package consists of integrated algorithms written in Fortran. The main aim of this software is to 'correct' (if needed) the pulse arrival times for the 'impurities' discussed in § 4.7.

We used TEMPO mainly for the barycentric correction purposes, although it takes care of the other corrections in an automated fashion. Although TEMPO is accompanied by insufficient documentation, the latest version called TEMPO2, is adequately documented. These documentation includes the detailed literature on TEMPO2 by Edwards et al. (2006) and (Hobbs et al., 2006).

TEMPO operates on the pulse arrival times that the user supplies in an input file. It then performs the necessary adjustments and produces an output file which contains the corrected arrival times. As such, TEMPO requires a fairly specific format of an input file — otherwise the user may receive error messages. Although we will show later, the auxiliary files included in the package may be helpful in creating the required format of the input file.

The use of TEMPO consist of several phases. First, after downloading and installing TEMPO (see Princeton (1997) for the procedures), the installed version needs some slight configurations before 'feeding' it with the observed ToAs. Then TEMPO will return an output file in some kind of format — which needs to be read out accordingly.

A.2 Preparing TEMPO

TEMPO can be downloaded on from Princeton (1997). Once downloaded, certain customization of TEMPO with respect to the user is needed.

For the timing corrections of the ToAs, TEMPO requires the position of the observatory on the surface of the Earth. A file by the name of `'obsys.dat'`, keeps record of the geographical locations of observatories. The contents in the `'obsys.dat'` file may look as follows:

5085442.778	2668263.49215	-2768697.04037	1	HARTRAO	j	HA
5622418.637	1665436.11212	-2505076.43426	1	H.E.S.S.	k	HE

where the first three *records*[1] gives the 3D (x,y,z) observatory coordinates in meters. The unity in the fourth record informs TEMPO that the position coordinates are given in meters, other than degrees. The last three records are the observatory name, number and code, respectively. The two-character observatory code is submitted along with each ToA in the input file — from which TEMPO reads the geographycal position coordinates of the site.

Note that each row in the `'obsys.dat'` file, represents an observatory. Therefore, it is an erroneous input if photon arrival times are submitted with the concerned observatory not listed in this file.

[1]It is tempting to used the term 'column' here. However, we reserve the concept of a column for later — when we will define the exact position of an record on a horizontal text line

A.3 TEMPO Input Data

The photon arrival times to be barycentered are passed on to TEMPO through an input file, that may only take certain prescribed formats. Various options of the so-called 'fixed' and 'free' formats are available (Princeton, 1997). These styles include the *Princeton format*, *the Parkes format* and the *ITOA format*. The ITOA free-format style was used in this work.

The free-format file, as used here, requires the list of input ToAs to be given below a few lines of pulsar descriptive information — these information is called the 'header'. That is to say, the ToAs follows a header in a file. A typical free-format input file may look like the image shown in Figure A.1 (in this case with only 5 ToAs):

```
 HEAD
 COORD J2000
 EPHEM DE405
# BINARY NONE
 NITS 0
 PSR 1509-58
 RA        15:13:55.62000002
 DEC       -59:08:09.0000001
# PMRA     -1.0000
# PMDEC    -0.1300
 PEPOCH    48355.000000
 POSEPOCH  48355.00
 DM        252.500000
 F0        6.6375697328
 F1        -6.7695374E-11
 F2        1.9587E-21
 P0        0.150657550919
 P1        1.53652913E-12
 CLK       UTC(NIST)

 TOA
1509-58  53089.1227881908      0.00 2.42e20       0.00000  HE
1509-58  53089.1228106720      0.00 2.42e20       0.00000  HE
1509-58  53089.1228188914      0.00 2.42e20       0.00000  HE
1509-58  53089.1228434714      0.00 2.42e20       0.00000  HE
1509-58  53089.1228500032      0.00 2.42e20       0.00000  HE
```

Figure A.1: *A sample of a ToA input file for TEMPO. The first few lines constitutes the 'header', followed by the word 'TOA' denoting the beginning of the list containing the pulse arrival times.*

The word 'HEAD' denotes the beginning of the header file as shown in Figure A.1. The header contains name of the ephemeris data base used (DE200 or DE405 designed for pulsar timing between the year 1950 and 2050), the pulsar name and position parameters, and the pulsar spin parameters with the respective epoch. More detail about the information in the header file can be seen in the *reference manual* obtainable from Princeton (1997). The user has to declare the following items in the header file (see sample in Figure A.1):

Item	Description
COORD	Type of coordinate system to be used
EPHEM	Empheris database to be used
BINARY	Binary system model if the pulsar is not isolated
NITS	Integer number of iterations, 0 for no repetition required
PSR	Pulsar name
RA	Right Ascension of object
DEC	Declination
PMRA	Proper motion in RA [in milli-arcsec per year)
PMDEC	Proper motion in DEC [in milli-arcsec per year)
PEPOCH	Epoch of pulsar parameters [in MJD]
POEPOCH	Epoch of pulsar position [in MJD]
DM	Dispersion measure [in pc/cm^3]
F0 (or F)	Pulsar frequency ν [in Hertz]
F1	First time derivative of the frequency $\dot{\nu}$ [in s^{-2}]
F2	Second time derivative of the frequency $\ddot{\nu}$ [in s^{-3}]
P0	Pulsar period [in seconds]
P1	First time derivative of the period [unitless]
CLK	Time system (clock) to use

Notice a typo (concerning the units) in the reference manual of Princeton (1997) where the abbreviation `F0` is explained — the units are erroneously given as $s-2$. The clock system defined as UTC(NIST) is the Coordinated Universal Time (UTC) kept and maintained by the National Institute of Standards and Technology (NIST) (see § 4.7.1). Note that statements that are commented out starts with the character '#'.

The list of pulse arrival times to be corrected start after the word 'TOA' — often referred to as the ToA lines. The first record thereafter, takes the form of the pulsar catalogue name (although this is optional) followed by the timing entry in MJDs. The third record in the ToA lines are the errors of the ToA values (ignored by TEMPO, in any case), while the observation frequency in MHz follows as the fourth record. The dispersion measure is entered as the fifth record in pc/cm^3, with the last record being the observatory code as define in the file 'obsys.dat'

Unlike in radio astronomy, the observation frequency for γ-ray data is not crucial — because the resulting dispersion measure as discussed in Chapter 4 has a negligible delay on the pulse arrival times. Nevertheless, the value of the observation frequency quoted in Figure A.1 is obtained from assuming a photon energy E of 1 Tev in the relation

$$\nu_{obs} = \frac{E}{h} \tag{A.1}$$

The entries in the `'obsys.dat'` file or in the ToA input file where deliberately considered as 'records', and not as column data. The reason for this probably dubious terminology originates from the fact that a *column*, in TEMPO input files, is defined as the position that a single character occupies on the horizontal text line. For example, the name *P B1509-58* occupies 10 consecutive columns — a single space takes occupies one column. With this definition, in TEMPO numbering columns starts from the extreme left (as column 1) of a horizontal text line to the right.

With this definition of a column in place, the records in the ToA lines of the input file (in ITOA format) must strictly be located at the following locations (see Princeton, 1997).

The ITOA Format of the input file	
Columns	**Record (Quantity)**
1-2	TEMPO ignores, but must not be blank (could put the pulsar name)
10-28	ToA (decimal point must be in column 15)
29-34	T0A uncertainty in microseconds, TEMPO ignores
35-45	Observing frequency in MHz
46-55	Dispersion measure in pc/cm^3
58-59	Observatory code defined in `'obsys.dat'`

Similarly, one can revisit the `'obsys.dat'` file, and say that the detail that was described in § A.2 must be placed at the following positions (see Princeton, 1997).

The observatory data file format	
Columns	**Record (Quantity)**
1-15	x-coordinate
16-30	y-coordinate
31-45	z-coordinate
48-48	put 1 for using meters for coordinates
51-62	Observatory name
71-71	Observatory number
74-75	Observatory code

Once the observatory data file (`'obsys.dat'`) and the input file with the ToAs (e.g. called `'1509-58obs1.dat'`) have been created and saved at the appropriate places, as described by the TEMPO reference manual, one can now do barycentric corrections by executing the following commands from the command line:

↪ navigate to the directory `tempo`
↪ navigate to the subdirectory `test`
↪ run the command `../src/tempo 1509-58obs1.dat`

The above commands instructs tempo to perform pulsar timing corrections, discussed in § 4.7, on the pulse arrival times given in the ToA lines of the file `'1509-58obs1.dat'`. The computational algorithms (written in Fortran) that do the theoretical calculations are in the `src` directory.

Upon successful completion of the procedure as described above, TEMPO creates a binary file (amongst others) that contains the barycentered ToAs in the `test` directory.

A.4 The TEMPO Output

In essence, there are about 8 output files (see Princeton (1997)), of which only two will be discussed — these are the files `'resid2.tmp'` and `'<psrname>.par'`

The file by the name `'<psrname>.par'` returns the pulsar parameters in ASCII format (basically a plain text file). The character `'<psrname>'` represents the pulsar catalogue name — for the example used in this text, this file will be named `'1509-58.par'`. The user can use this parameter file for re-confirmation of the submitted pulsar ephemerides, or alternatively for future input files. A sample of a complete `'<psrname>.par'` file is shown in Figure A.2

```
PSR              1509-58
RAJ        15:13:55.62000004
DECJ       -59:08:09.0000002
POSEPOCH         48355.0000
F0       6.6375697328000003
F1      -6.769537400000E-11
F2       1.958700000000E-21
PEPOCH         48355.000000
START            53089.122
FINISH           53089.155
DM              252.500000
EPHEM              DE405
CLK              UTC(NIST)
NTOA                2883
TRES              43045.13
TZRMJD   53089.12278820259442
TZRFRQ ********************
TZRSITE                   k
```

Figure A.2: *A sample of a TEMPO output file with pulsar parameters. This file is named* `'<psrname>.par'`*, where the part* `'<psrname>'` *represents the catalogue name of the pulsar.*

Perhaps the most needed output of TEMPO is the file, `'resid2.tmp'`, that contains the barycentered (or corrected) pulse arrival times. Unfortunately, this file does not come in plain text format — it is a binary file. TEMPO does not

provide the tools for reading the contents of this file, but gives the overall structure of the contents of **'resid2.tmp'**. These in essence informs the user of the type of records or quantities that are in the file.

The author employed the C code shown in Figure A.3. This programme reads into the **'resid2.tmp'** binary file, extracts the information in there, and write it onto a plain text format file called **'output.dat'**

```
// This code reads the binary file "resid2.tmp", which is the output file
// from TEMPO after barycentering.

// Developed by ID Davids with the assistance from Paulus Kruger (both from
// the North-West University, Potchefstroom, South Africa)

// Completed on 27/01/2006

#include <stdio.h>
#include <stdlib.h>

int main()
{

FILE *fin,*fout;                    // Create pointers for the output file &
                                    // for the file were the extracted ToAs will
                                    // be written

fin = fopen("resid2.tmp","rb"); // The binary file to open for reading
fout = fopen("output.dat","w"); // The data file to write on

double *record;
float tmp;

record = (double*)calloc(9,sizeof(double));

int i;
int num_records;
num_records = 2113;                 // Change this value to the number of time
                                    // stamps in observation
num_records = num_records - 1;      // For some reason TEMPO outputs are 1 less
                                    // then inputs

float size=2*sizeof(float)+9*sizeof(double);
//printf("%le",size);
    for (i = 0; i < num_records; i++)
    {
      fread(&tmp,sizeof(float),1,fin);
      fread(record,sizeof(double),9,fin);
      fread(&tmp,sizeof(float),1,fin);
      fprintf(fout,"%1.15e      %1.5e   %1.5e   %1.3e   %1.3e   %1.3e   %1.3e   %1.3e
%1.3e\n",record[0],record[1],record[2],record[3],record[4],record[5],record[6],record[7],re
cord[8]);
    }

fclose(fin);
fclose(fout);

return 0;
}
```

Figure A.3: *A C programme for reading TEMPO's binary output file. This code reads the file* **'resid2.tmp'**, *and write its contents onto a text file called* **'output.dat'**.

The values that are read from TEMPO's output are written onto a file that is readily accessible. In these case, this new file created was called **'output.dat'** — created by the algorithm shown in Figure A.3. Figure A.4 shows a sample of the first five lines of **'output.dat'**.

In Figure A.4 the first record gives the barycentered ToAs expressed in MJD format. The user can then extract these ToAs for further γ-ray analysis. The second, third, and the eight records gives the *residuals* of the timing

data. A residual is the difference in the observed pulse arrival time and the expected pulse arrival time. TEMPO does some fitting on the residuals, and shows the pre-fit residual in the eight record, while the second and the third records carry the post-fit residuals in terms of the phase and in seconds, respectively (see Princeton (1997)). The fourth record shows the orbital phase, with the observing frequency given as the fifth record. The so-called weight of the point, always obtained as unity, is given in the sixth record. The uncertainty on the pulse arrival time comes as the seventh record, while the ninth record seems redundant.

In these work, the only quantity of interest are the pulse arrival times. For these reason, although it has many other usages, TEMPO was only utilized for doing barycentric correction of the pulse arrival times. As such, only the first entry in each row of data in Figure A.4 were carried forward for periodicity search tests.

```
5.308912581653264e+04 -6.76394e-03 -1.01904e-03 0.000e+00 2.420e+20 1.000e+00 0.000e+00  0.000e+00 0.000e+00
5.308912583901534e+04 -1.66721e-01 -2.51178e-02 0.000e+00 2.420e+20 1.000e+00 0.000e+00 -1.600e-01 0.000e+00
5.308912584723529e+04 -4.72245e-01 -7.11473e-02 0.000e+00 2.420e+20 1.000e+00 0.000e+00 -4.655e-01 0.000e+00
5.308912587181692e+04 -4.33481e-01 -6.53072e-02 0.000e+00 2.420e+20 1.000e+00 0.000e+00 -4.267e-01 0.000e+00
5.308912587834915e+04  2.97129e-01  4.47647e-02 0.000e+00 2.420e+20 1.000e+00 0.000e+00  3.039e-01 0.000e+00
```

Figure A.4: *A sample of a segment of TEMPO's output data. This information is originally contain in a binary file. The record on the first from left, gives the barycentered pulse arrival times in MJD format. The remaining records include various residuals — not essential for this work.*

Appendix B

Error Analysis

IN any observational or otherwise experimental data analysis it is imperative to know the magnitudes of the errors that are associated with the measurements and the computations. Obtained numerical values should be accompanied by a reasonable estimate of the level of confidence associated with the measured quantity. Evaluation of the quality of the experimental results are dependent on the magnitudes of the corresponding uncertainties. Without an uncertainty estimate, it is not sensible to decide if a scientific hypothesis is confirmed or invalidated. Thus, for the a meaningful final evaluation of the stated hypotheses, in the periodicity search that we carried out, it became essential to have a feeling of the associated errors.

B.1 Error Propagation in Expected Period

in what follows, compute the errors on the values of expected periods used in the Rayleigh test. By doing this for the different observations we can comment on the time dependency of the evolution of these errors.

Let us define the error in a quantity x to be δx, such that we can summarize the pulsar frequency and its time derivatives (with the associated uncertainties) as follows:

$$\begin{aligned}
\nu \pm \delta\nu &= (6.6375697328 \pm 8 \times 10^{-10})s^{-1} \\
&= (6.6375697328 \pm 0.0000000008)s^{-1} \\
\dot{\nu} \pm \delta\dot{\nu} &= (-6.7695374 \times 10^{-11} \pm 4 \times 10^{-18})s^{-2} \\
&= (-6.7695374 \pm 0.0000004) \times 10^{-11}s^{-2} \\
\ddot{\nu} \pm \delta\ddot{\nu} &= (1.9587 \times 10^{-21} \pm 9 \times 10^{-25})s^{-3} \\
&= (1.9587 \pm 0.0009) \times 10^{-21}s^{-3} \\
\dddot{\nu} \pm \delta\dddot{\nu} &= (-1.02 \times 10^{-31} \pm 2.5 \times 10^{-32})s^{-4} \\
&= (-1.02 \pm 0.25) \times 10^{-31}s^{-4}
\end{aligned}$$

From the calculation of the expected radio frequency as

$$\nu_{expt} = \nu + \nu' \cdot (ToA_{min} - T_{ref}), \tag{B.1}$$

with $ToA_{min} - T_{ref}$ considered as exact, we can deduce the corresponding error in the expected radio frequency as

$$\delta\nu_{expt} = \sqrt{(\delta\nu)^2 + (\delta\nu' \cdot (ToA_{min} - T_{ref}))^2}. \tag{B.2}$$

Since we get the expected radio period by the inversion relation

$$P_{expt} = \frac{1}{\nu_{expt}} \tag{B.3}$$

we infer that the approximate uncertainty in the expected radio period is

$$\delta P_{expt} = \frac{\delta \nu_{expt}}{\nu^2_{expt}}. \tag{B.4}$$

Finally, one can then quote the expected radio period with the associated uncertainty as

$$P_{expt} = \frac{1}{\nu_{expt}} \pm \frac{\delta \nu_{expt}}{\nu^2_{expt}} \tag{B.5}$$

By virtue of Equation B.5, we noticed that the uncertainty in P_{expt} is of order 4×10^{-11} s. For example, the period expected at the first night of observation of MSH15-52 is:

P_{expt} = (1.512886678519588e-01 $\pm$ 4.1685×10^{-11})s = (0.151288667851 $\pm$ 0.000000000042)s.

If each night is treated separately, then the expected period with an error estimate, can be quoted for all 23 nights of observations — this is shown in Table B.1.

Data set	Expected period & its error [s]
Night 1	$0.151288667851959 \pm 4.1685\times10^{-11}$
Night 2	$0.151291326358576 \pm 4.1827\times10^{-11}$
Night 3	$0.151291460557072 \pm 4.1835\times10^{-11}$
Night 4	$0.151291593892070 \pm 4.1842\times10^{-11}$
Night 5	$0.151291726462323 \pm 4.1849\times10^{-11}$
Night 6	$0.151291861361101 \pm 4.1856\times10^{-11}$
Night 7	$0.151291996045285 \pm 4.1863\times10^{-11}$
Night 8	$0.151292127702712 \pm 4.1870\times10^{-11}$
Night 9	$0.151292262050551 \pm 4.1878\times10^{-11}$
Night 10	$0.151292394650845 \pm 4.1885\times10^{-11}$
Night 11	$0.151298810114107 \pm 4.2230\times10^{-11}$
Night 12	$0.151299475649161 \pm 4.2265\times10^{-11}$
Night 13	$0.151299601636389 \pm 4.2272\times10^{-11}$
Night 14	$0.151299728299088 \pm 4.2279\times10^{-11}$
Night 15	$0.151299868045196 \pm 4.2286\times10^{-11}$
Night 16	$0.151300009209486 \pm 4.2294\times10^{-11}$
Night 17	$0.151300409296480 \pm 4.2316\times10^{-11}$
Night 18	$0.151303345808825 \pm 4.2474\times10^{-11}$
Night 19	$0.151303477898720 \pm 4.2481\times10^{-11}$
Night 20	$0.151303612646303 \pm 4.2488\times10^{-11}$
Night 21	$0.151303755313229 \pm 4.2496\times10^{-11}$
Night 22	$0.151304018290757 \pm 4.2510\times10^{-11}$
Night 23	$0.151304292257411 \pm 4.2525\times10^{-11}$

Table B.1: *The night-wise expected periods and the associated errors. These assumes extrapolation of the radio period to the respective night. These errors are negligible, so that the graphs given in the text have no error bars — the error bars would be smaller than the data points.*

B.2 A Comment on the Errors

The error of the pulsar period δP at the ephemeris epoch is given as 1.9×10^{-11} by Kaspi et al. (1994) and the ATNF Pulsar Catalogue. Hence, we notice an increase by a factor of ~ 2 when we compute δP_{expt}. However, the errors are quite small as they only contribute to the uncertainty from the 11th decimal digit of the period onwards.

The minuteness of the errors favours the Rayleigh- and the H-tests. The IFS in the test is much larger than the errors on the periods. For the smallest IFS, corresponding to the aggregate data set we have

$$\delta P \sim 10^{-11} \ll 10^{-8} \sim IFS \tag{B.6}$$

The uncertainty on the period δP is much smaller than the IFS that we are searching in. The error bars on the periodograms would be too small to indicate on the graphs. Thus, the error on the period values can be neglected in this work.

Bibliography

Aharonian, F. A., ed. 2004, Very High Energy Cosmic Gamma Radiation (London: World Scientific Publishing)

Aharonian, F. A. et al. 2005a, A&A, 435, L17

—. 2006a, pre-print (astro-ph/0607333)

—. 2005b, A&A, 432, L25

—. 2006b, pre-print (astro-ph/0601575)

—. 2006c, pre-print (astro-ph/0606311)

—. 2006d, Search for Pulsed VHE γ-ray Emission from Young Pulsars with H.E.S.S., to be published in A&A

Aharonian, F. A., & Konopelko, A. K. 1997, pre-print (astro-ph/9712044)

Amato, E. 2003, Chin. J. Astron. Astrophys., 3, 316

Berger, J. O., Boukai, B., & Wang, Y. 1997, Statist. Sci, 12, 133

Brazier, K. T. S. 1994, MNRAS, 268, 709

Brown, A. M., Chadwick, P. M., Dickinson, H. J., Hadjichristidis, C., Latham, I. J., & Le Gallou, R. 2005, in 29th Int. Cosmic Ray Conf. (Pune, India), 411

Buccheri, R. et al. 1983, A&A, 128, 245

Caswell, J. L., Milne, D. K., & Wellington, K. J. 1981, MNRAS, 195, 89

Chadwick, P. M., Lyons, K., McComb, T. J. L., Orford, K. J., Osborne, J. L., Rayner, S. M., Shaw, S. E., & Turver, K. E. 2000, in American Institute of Physics Conference Series, ed. M. L. McConnell & J. M. Ryan, 168

Cheng, K. S., Ho, C., & Ruderman, M. 1986, ApJ, 300, 500

Cordes, J. M., & Helfand, D. J. 1980, ApJ, 239, 640

Cox, N. J. 2001, Analysing Circular Data in Stata, North American Stata Users' Group Meetings 5.3

Daugherty, J. K., & Harding, A. K. 1982, ApJ, 252, 337

de Jager, O. C. 1987, PhD thesis, Faculty of Natural Sciences, Potchefstroom University of Christian Higher Education, South Africa

de Jager, O. C., Raubenheimer, B. C., & Swanepoel, J. W. H. 1989, A&A, 221, 180

DURHAM-Group. 2006, Very High Energy Gamma Rays from Cen X-3, http://www.dur.ac.uk/~dph0www4/papers/daniel.pdf (Date of access: 24 Nov. 2006)

Eadie, W. T., Drijard, D., & James, F. E. 1971, Statistical methods in experimental physics (Amsterdam: North-Holland Publishing Company)

Edwards, R. T., Hobbs, G. B., & Manchester, R. N. 2006, MNRAS, 372, 1549

Frescura, F. A. M. 2002, African Skies, 7, 34

Gaensler, B. M., Arons, J., Kaspi, V. M., Pivovaroff, M. J., Kawai, N., & Tamura, K. 2002, ApJ, 569, 878

Gaensler, B. M., & Slane, P. O. 2006, pre-print (astro-ph/0601081)

Gallant, Y. A. 2006, pre-print (astro-ph/0611720)

Goldreich, P., & Julian, W. H. 1969, ApJ, 157, 869

Greenwald, A. G. 1975, Psychological Bulletin, 82, 1

Guttman, L. 1977, The Statistician, 26, 81

Gvaramadze, V. V. 2001, A&A, 374, 259

Hartle, J. B. 2003, Gravity: An Introduction to Einstein's General Relativity (San Francisco: Addison Wesley)

Hillas, A. M. 1996, Space Sci. Rev., 75, 17

Hinton, J. A. 2004, New Astronomy Review, 48, 331

Hobbs, G. B., Edwards, R. T., & Manchester, R. N. 2006, MNRAS, 369, 655

Hofmann, W. et al. 2000, Astropart. Phys., 13, 253

Jelley, J. V., & Porter, N. A. 1963, QJRAS, 4, 275

Johnstone, D. J., Barnard, G. A., & Lindley, D. V. 1986, The Statistician, 35, 491

Kaspi, V. M., Manchester, R. N., Siegman, B., Johnston, S., & Lyne, A. G. 1994, ApJ, 422, L83

Kawaler, S. D., Novikov, I., & Srinivasan, G. 1997, in Saas-Fee Advanced Course 25, Lecture Notes 1995: Stellar Remnants, ed. S. D. Kawaler, I. Novikov, & G. Srinivasan, 23

Khélifi, B. 2005, in SF2A-2005: Semaine de l'Astrophysique Francaise, ed. F. Casoli, T. Contini, J. M. Hameury, & L. Pagani, 237

Khélifi, B., Masterson, C., & Hinton, J. 2005, in 29th Int. Cosmic Ray Conf. (Pune, India), 4, 127

Konopelko, A. et al. 2005, in 29th Int. Cosmic Ray Conf. (Pune, India), 4, 101

Kundt, W., ed. 2004, Astrophysics: a new approach (Germany: Springer)

Lemoine-Goumard, M., Degrange, B., & Tluczykont, M. 2006, Astropart. Phys., 25, 195

Lewis, D. A. 1989, A&A, 219, 352

Lindley, D. V. 2000, The Statistician, 49, 293

Livingstone, M. A., Kaspi, V. M., Gavriil, F. P., & Manchester, R. N. 2005, ApJ, 619, 1046

Lynden-Bell, D., & Rees, M. J. 1971, MNRAS, 152, 461

Lyne, A. G., & Graham-Smith, F. 1990, Pulsar Astronomy (Cambridge: Cambridge University Press)

Manchester, R., Hobbs, G., Teoh, A., & Hobbs, M. 2004, pre-print (astro-ph/0412641)

Manchester, R. N., & Taylor, J. H. 1977, Pulsars (San Francisco: W. H. Freeman)

Mardia, K. K., & Jupp, P. E. 1999, Directional Statistics (Chichester: John Wiley & Sons Ltd)

NASA. 2006, Introduction to Supernova Remnants, http://heasarc.gsfc.nasa.gov/docs/objects/snrs/snrstext.html (Date of access: 3 Aug. 2006)

NIST. 2006, Time and Frequency Division, http://tf.nist.gov/general/precision.htm (Date of access: 27 Nov. 2006)

Oña-Wilhelmi, E. M., & de Jager, O. C. 2002, African Skies, 7, 30

Paltani, S. 2004, A&A, 420, 789

Pratap, P., & McIntosh, G. 2005, Am. J. Phys., 73, 399

Princeton. 1997, TEMPO, http://pulsar.princeton.edu/tempo/tempo_idx.html (Date of access: 7 Dec. 2006)

Reynoso, E. M., Green, A. J., Johnston, S., Goss, W. M., Dubner, G. M., & Giacani, E. B. 2004, Publications of the Astronomical Society of Australia, 21, 82

Schlenker, S. 2005, presentation at the SPP Meeting of 2nd December 2005

Schmidt, F. 2005, presentation at the Workshop on Pulsars and SNRs, Berlin

Seward, F. D., & Harnden, Jr., F. R. 1982, ApJ, 256, L45

Shklovskii, I. S. 1978, Stars: their birth, life, and death (San Francisco: W. H. Freeman)

Spitkovsky, A. 2005, in AIP Conf. Proc. 801: Astrophysical Sources of High Energy Particles and Radiation, ed. T. Bulik, B. Rudak, & G. Madejski, 253

Tayler, R. J. 1994, The Stars: Their structure and evolution (2d ed.; Cambridge: Cambridge University Press)

Tiplady, A. J., & Frescura, F. A. M. 2002, African Skies, 7, 12

Ueno, A. 2005, PhD thesis, Department of Physics, Graduate School of Science, Kyoto University

Urama, J. O. 2002a, MNRAS, 330, 58

—. 2002b, African Skies, 7, 18

USC. 2006, Chi Squared Calculator, http://rockem.stat.sc.edu/prototype/calculators/ (Date of access: 21 Nov. 2006)

Vincent, P. 2005, in 29th Int. Cosmic Ray Conf. (Pune, India), 5, 331

Weekes, T. C. 2005, pre-prints (astro-ph/0508253)

Wikipedia. 2006a, Anthony Hewish, http://en.wikipedia.org/wiki/Anthony_Hewish (Date of access: 2 Aug. 2006)

—. 2006b, Degrees of Freedom, http://en.wikipedia.org/wiki/Degrees_of_freedom (Date of access: 11 Dec. 2006)

—. 2006c, Interplanetary Scintillation Array, http://en.wikipedia.org/wiki/Interplanetary_Scintillation_Array (Date of access: 2 Aug. 2006)

—. 2006d, Magnetar, http://en.wikipedia.org/wiki/Magnetar (Date of access: 4 Aug. 2006)

—. 2006e, Neutron Star, http://en.wikipedia.org/wiki/Neutron_star (Date of access: 3 Aug. 2006)

—. 2006f, Pavel Alekseyevich Cherenkov, http://en.wikipedia.org/wiki/Pavel_Alekseyevich_Cherenkov (Date of access: 2 Aug. 2006)

—. 2006g, Supernovae, http://en.wikipedia.org/wiki/Supernovae (Date of access: 3 Aug. 2006)

Yatsu, Y., Kawai, N., Kataoka, J., Tamura, T., & Brinkmann, W. 2006, in ESA SP-604: The X-ray Universe 2005, ed. A. Wilson, 379